NASA Contractor Report 172299

(NASA-CR-172299) NONLINEAR POTENTIAL ANALYSIS TECHNIQUES FOR SUPERSONIC-HYPERSONIC AERODYNAMIC DESIGN (Rockwell International Science Center) 57 p HC A04/MF A01 CSCL 01A G3/02

N86-23569

Unclas 06037

Nonlinear Potential Analysis Techniques for Supersonic/ Hypersonic Aerodynamic Design

V. Shankar and W. C. Clever

ROCKWELL INTERNATIONAL CORPORATION
Los Angeles, California 90009

CONTRACT NAS1-15820
7 MARCH 1984

MAY 1986
PUBLICLY RELEASED
ON

NASA
National Aeronautics and Space Administration

Langley Research Center
Hampton, Virginia 23665

1. Report No.	2. Government Accession No.	3. Recipient's Catalog No.
NASA CR-172299		

4. Title and Subtitle	5. Report Date
NONLINEAR POTENTIAL ANALYSIS TECHNIQUES FOR SUPERSONIC/ HYPERSONIC AERODYNAMIC DESIGN	March 7, 1984
	6. Performing Organization Code NA-83-1161
7. Author(s) V. Shankar and W. C. Clever	8. Performing Organization Report No.
	10. Work Unit No.
9. Performing Organization Name and Address Rockwell International P. O. Box 92098 Los Angeles, California 90009	11. Contract or Grant No. NAS1-15820
	13. Type of Report and Period Covered Contractor report
12. Sponsoring Agency Name and Address National Aeronautics and Space Administration Langley Research Center Hampton, Virginia 23665	14. Sponsoring Agency Code

15. Supplementary Notes

Technical monitors: Noel A. Talcott, Jr. and Kenneth M. Jones

16. Abstract

Approximate nonlinear inviscid theoretical techniques for predicting aerodynamic characteristics and surface pressures for relatively slender vehicles at supersonic and moderate hypersonic speeds were developed. Emphasis was placed on approaches that would be responsive to conceptual configuration design level of effort. Second order small disturbance and full potential theory was utilized to meet this objective.

Numerical codes were developed for relatively general three dimensional geometries to evaluate the capability of the approximate equations of motion considered. Results from the computations indicate good agreement with experimental results for a variety of wing, body, and wing-body shapes.

17. Key Words (Suggested by Author(s))	18. Distribution Statement
Aerodynamic theory Potential analysis Supersonic/hypersonic	[redacted]

19. Security Classif. (of this report)	20. Security Classif. (of this page)	21. No. of Pages	22. Price
Unclassified	Unclassified	51	

[redacted]

NASA Contractor Report 172299

NONLINEAR POTENTIAL ANALYSIS TECHNIQUES FOR SUPERSONIC/ HYPERSONIC AERODYNAMIC DESIGN

V. Shankar and W. C. Clever

ROCKWELL INTERNATIONAL CORPORATION
Los Angeles, California 90009

CONTRACT NAS1-15820
MARCH 7, 1984

FOREWORD

This final report was prepared by the Los Angeles Aerodynamic Group and the Science Center of Rockwell International, Los Angeles, California for the Langley Research Center, National Aeronautics and Space Administration, Hampton, Virginia. The work was performed under Contract No. NAS1-15820, "Development of Second Order Potential Analysis/Design and Full Potential Analysis Aero Prediction Technology for Hypersonic Configuration Design." Mr. Noel Talcott and Mr. Kenneth Jones were the Project Monitors of this contract.

Mr. E. Bonner was the Program Manager; Drs. V. Shankar and W. C. Clever were the Principal Investigators.

SUMMARY

Approximate nonlinear inviscid theoretical techniques for predicting aerodynamic characteristics and surface pressures for relatively slender vehicles at supersonic and moderate hypersonic speeds were developed. Emphasis was placed on approaches that would be responsive to conceptual configuration design level of effort. Second order small disturbance and full potential theory was utilized to meet this objective.

Numerical codes were developed for relatively general three dimensional geometries to evaluate the capability of the approximate equations of motion considered. Results from the computations indicate good agreement with experimental results for a variety of wing, body, and wing-body shapes.

PRECEDING PAGE BLANK NOT FILMED

TABLE OF CONTENTS

		Page
1.	INTRODUCTION	1
2.	LIST OF SYMBOLS	2
3.	METHODOLOGY	4
4.	SECOND ORDER POTENTIAL ANALYSIS/DESIGN	5
	4.1 Geometry	5
	4.2 Input/Output Graphics	5
5.	FULL POTENTIAL ANALYSIS	10
	5.1 Geometry	10
	5.2 Wake Model	10
	5.3 Sideslip	11
6.	RESULTS	17
	6.1 Second Order	17
	6.2 Full Potential	22
7.	CONCLUSIONS	26
8.	REFERENCES	27
APPENDIX A	CONTRACT PUBLICATIONS	28

PRECEDING PAGE BLANK NOT FILMED

1. INTRODUCTION

An examination of the literature for supersonic/hypersonic aircraft provides an indication of the flexibility and generality required for a prediction technique. Typical configuration development variables include wing section, incidence, height, dihedral, planform, effectiveness of longitudinal control surfaces for trim, effectiveness of empennage for directional stability, and propulsion system-airframe interactions.

State-of-the-art response to these prediction requirements is provided by hypersonic impact methods as well as linearized analysis and design algorithms. These approaches can treat complex geometries with minimum response time and cost, with efficient predicted data coverage in terms of Mach number, angle of attack, trim deflection, yaw angle, etc. Shortcomings are present, however, in both the impact and linearized methods. For the former, interference between surface elements is totally ignored in implementations such as classicial Newtonian, tangent wedge, and cone theories. Cross-flow interactions and stagnation point singularities are also implicitly disregarded. In the latter, shocks, vorticity, and entropy wakes and layers are excluded. Furthermore, superposition of elementary solutions such as those for thickness and angle of attack freely used in linear models are, strictly speaking, invalid at hypersonic speeds.

A need exists for new aerodynamic prediction techniques to optimize vehicles designed to travel at supersonic/hypersonic speeds. One requirement of a new aerodynamic prediction technique is that it be more accurate than simple noninterfering panel methods. Another specification is that it be more computationally efficient than currently available explicit finite-difference methods so that it can be incoporated into a practical design procedure. The new approach should include enough of the physics of the flow to allow realistic optimization and should permit consideration of appropriate interactions between components of promising arrangements, since this has been found to be the key to increasing aerodynamic efficiency using linear methodology. Nonlinear potential theoretical formulations hold the promise of meeting this objective and providing economic design codes which are responsive to conceptual vehicle definition efforts.

2. LIST OF SYMBOLS

AR	aspect ratio, b^2/S
b	wing span
c	chord
$\bar{c}$	mean aerodynamic chord
C_D	drag coefficient, $D/q_\infty S$
C_L	lift coefficient, $L/q_\infty S$
C_m	pitching moment coefficient, $M/q_\infty S\bar{c}$
C_p	pressure coefficient, $\frac{P-P_\infty}{q_\infty}$
C_Z	normal force coefficient, $Fy/q_\infty S$
d	body maximum diameter
D	drag
F	force
ℓ	body length
L	lift
M	Mach number or moment
P	static pressure
q	dynamic pressure
S	reference area
u,v,w	axial, vertical, and lateral perturbation velocity
x,y,z	axial, vertical, lateral body axis cartesian coordinate
α	angle of attack
β	sideslip angle
ζ,η,ξ	see figures 5.2 and 5.3
Θ	polar angle
ϕ	velocity potential
[ ]	denotes jump
λ	taper ratio, c_t/c_r
Λ	sweep

SUBSCRIPTS

ac	aerodynamic center
LE	leading edge
r	root
t	tip or maximum thickness
x,y,z	component in x,y,z direction respectively
α	angle of attack
∞	freestream

3. METHODOLOGY

Emphasis is placed on approximate theoretical approaches which are capable of treating relatively general three dimensional problems but still sufficiently simple to be responsive to vehicle conceptual design efforts. The basic intent of the methodology is to produce improvement in lift-drag ratio of supersonic/hypersonic cruise vehicles. As a result of the strong impact that favorable interference has had on supersonic design and the use of such concepts in recent advanced hypersonic aircraft studies, candidate analysis should be general enough to systematically treat such problems. Finally, interest in high aerodynamic efficiency emphasizes relatively slender configurations at modest attitude; that is, moderate values of the hypersonic similarity parameter.

Prior theoretical effort [1-3] has advanced the supersonic/hypersonic aerodynamic prediction state-of-the-art at the conceptual design level. Numerical second-order potential small disturbance analysis was developed as a first step up from the widely used linear theory. Such a formulation incorporates nonlinear behavior by iteration of the Prandtl-Glauert approximation. This approach is known to extend the prediction success for airfoil and cone surface pressure to substantially higher values of the hypersonic similarity parameter than the first-order theory. The next level of theoretical richness vis-a-vis a full-potential equation of motion formulation was explored in parallel. This analysis eliminates edge singularities and improves treatment of characteristic surfaces but still retains isentropic assumption.

Hypersonic small disturbance theory was considered in an earlier study[1] in recognition of the progressive non-isentropic behavior of the flow as the value of the hypersonic similarity parameter increases. Finite difference analysis of this approximation[4] indicated that the solution was essentially as complex as that for the Euler equation and thus would not be particularly responsive to conceptual design level of effort. This approach was not pursued in the present study on the basis of this finding and the previously cited success of potential analysis at moderate hypersonic conditions.

ORIGINAL PAGE IS
OF POOR QUALITY

4. SECOND ORDER DESIGN/ANALYSIS

The second-order analysis[1,2] and design[3] codes developed under this contract are based on correcting the three-dimensional first-order potential solution, ϕ, for the dominant contributions of the nonhomogeneous Prandtl-Glauert equation

$$\Box^2 \phi^{(2)} = M_\infty^2 \frac{\partial}{\partial x} \left\{ \left[(1-M_\infty^2) + \frac{\gamma+1}{2} M_\infty^2 \right] \phi_x^2 + \phi_y^2 + (\phi_z + \alpha_\infty)^2 \right\}$$

where

$$\Box^2 \phi = \left\{ (1-M_\infty^2) \frac{\partial^2}{\partial x^2} + \frac{\partial^2}{\partial y^2} + \frac{\partial^2}{\partial z^2} \right\} \phi = 0$$

and associated surface boundary conditions. The local surface pressure coefficient has the form

$$C_p = C_p^{(1)} + C_p^{(2)}$$

where the superscripts refer to the first- and second-order contributions, respectively.

4.1 GEOMETRY

The Aerodynamic Preliminary Analysis System (APAS)[5,6] was interfaced with the second order analysis code to achieve general configuration modeling since it provides a well automated interactive capability. Modifications of variables such as surface planform, component location, incidence, dihedral, etc are easily accomplished through use of system interactive commands. A typical APAS aircraft model is presented on figure 4.1 to illustrate the geometric generality available.

4.2 INPUT/OUTPUT GRAPHICS

The responsiveness of aerodynamic analysis at the conceptual design level is dependent on the ability to verify modeling and review/collate solution results for a large number of parametric configuration variables in a timely manner. The use of graphics to display and examine geometry paneling minimizes modeling errors and associated erroneous analysis. Typical graphical finite element configuration definition is presented on figure 4.2 for a wing-body-canard arrangement.

Review and comparison of the local characteristics is used to assess the impact of parametric geometry modification. Chordwise distribution of surface pressure and the spanwise variation of typical sectional characteristics such as lift, drag, leading edge thrust, center of pressure, etc may be displayed for this purpose. A typical set of output is presented on figure 4.3.

ORIGINAL PAGE IS
OF POOR QUALITY

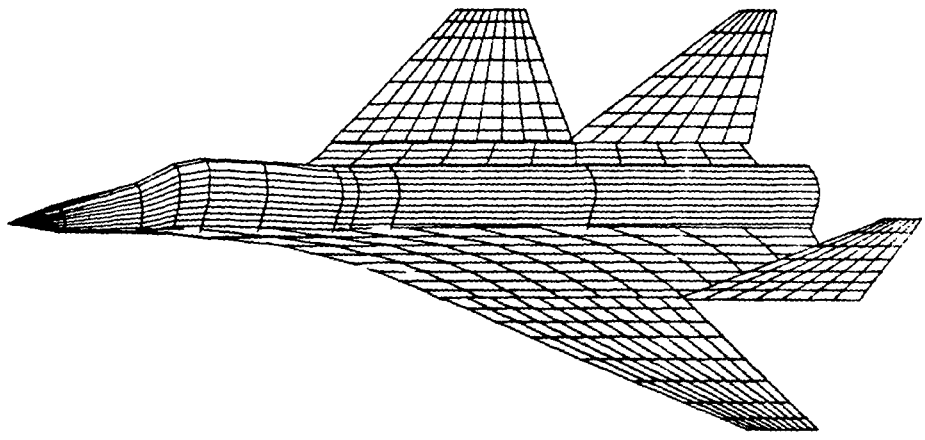

Figure 4.1. Typical APAS Aircraft Model

ORIGINAL PAGE IS
OF POOR QUALITY

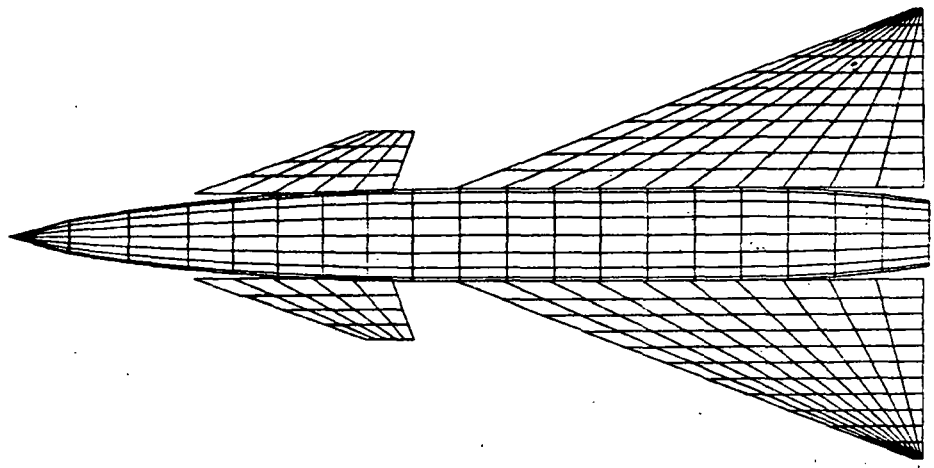

a) Plan View

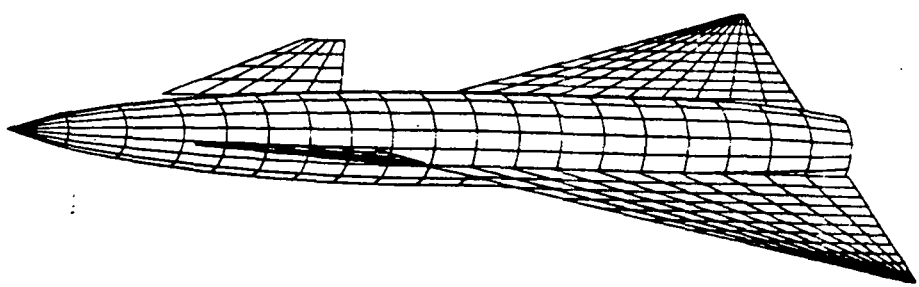

b) Orthographic View

Figure 4.2 Typical Finite Element Model Graphics

ORIGINAL PAGE IS
OF POOR QUALITY

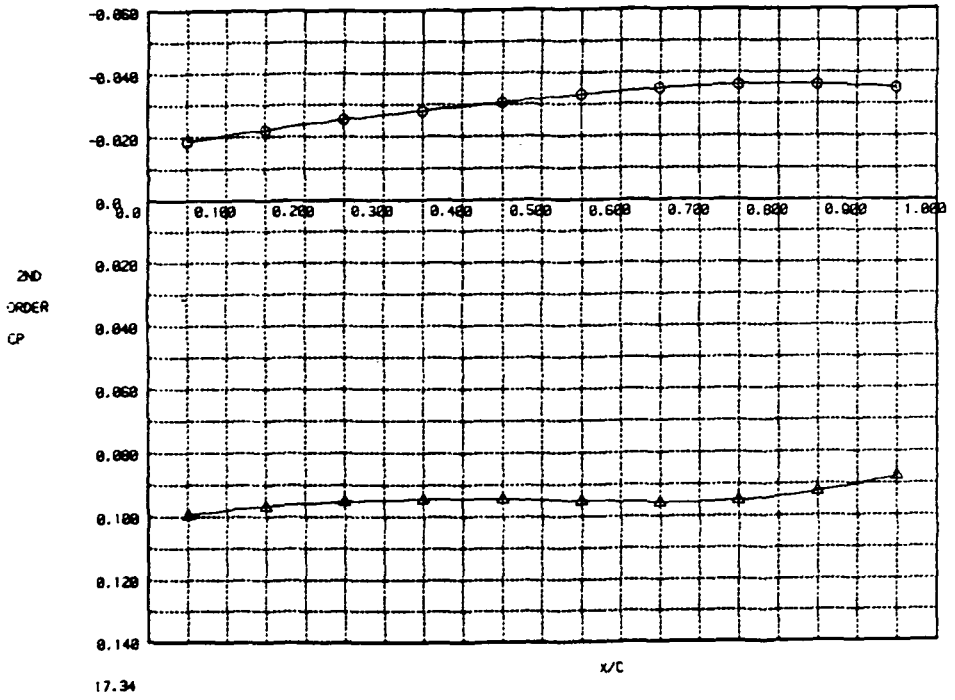

a) Chordwise Pressure Distribution

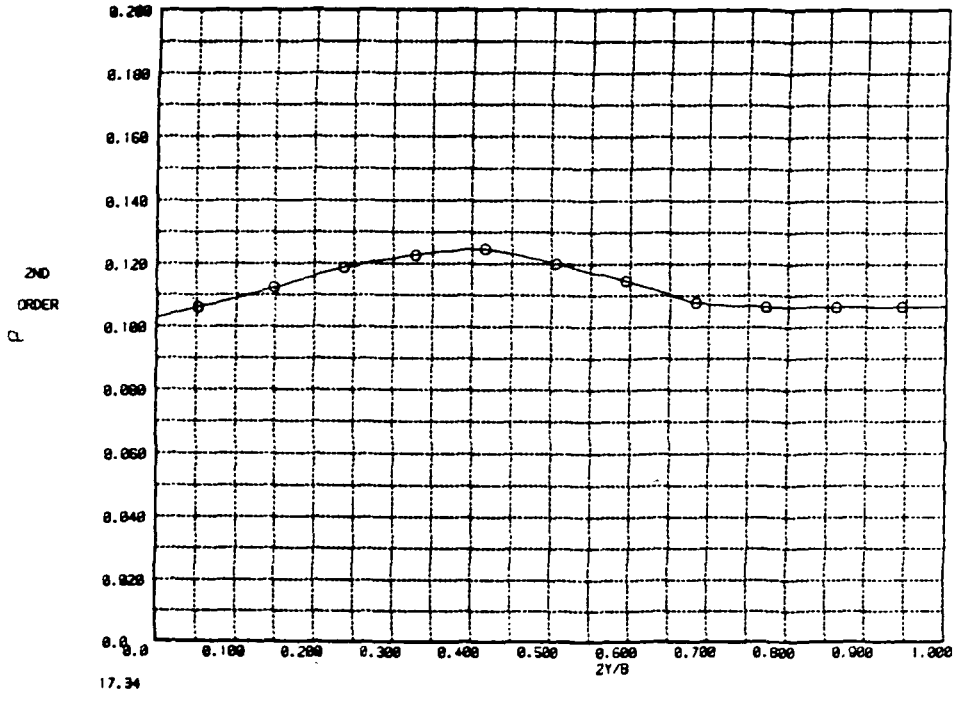

2z/b

b) Sectional Lift

Figure 4.3 Typical Aerodynamic Analysis Graphics

ORIGINAL PAGE IS
OF POOR QUALITY

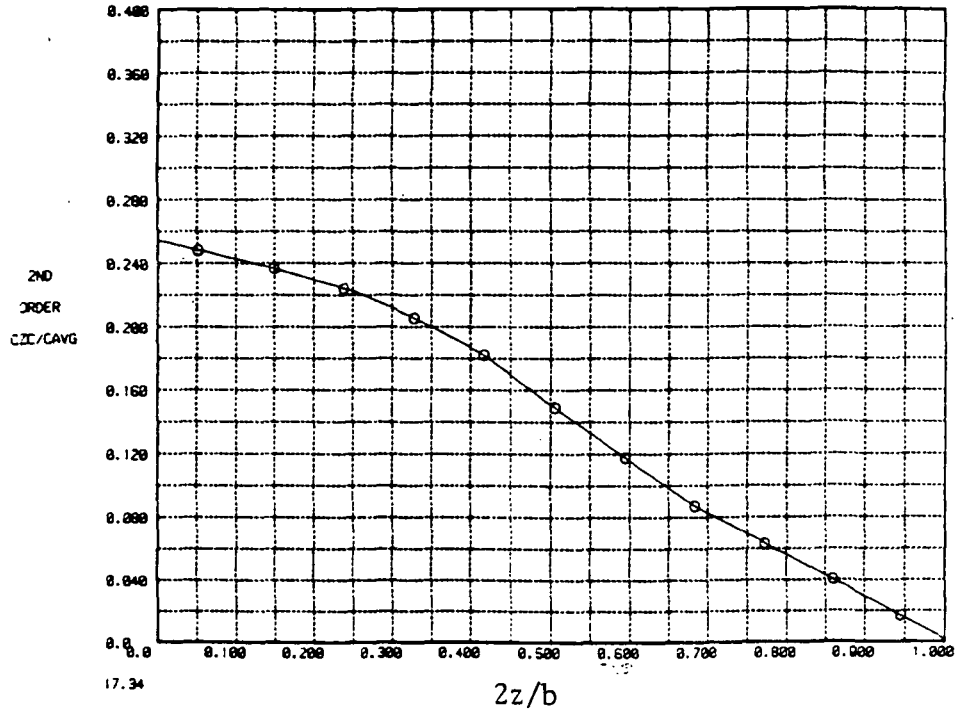

c) Chord Weighted Sectional Normal Force

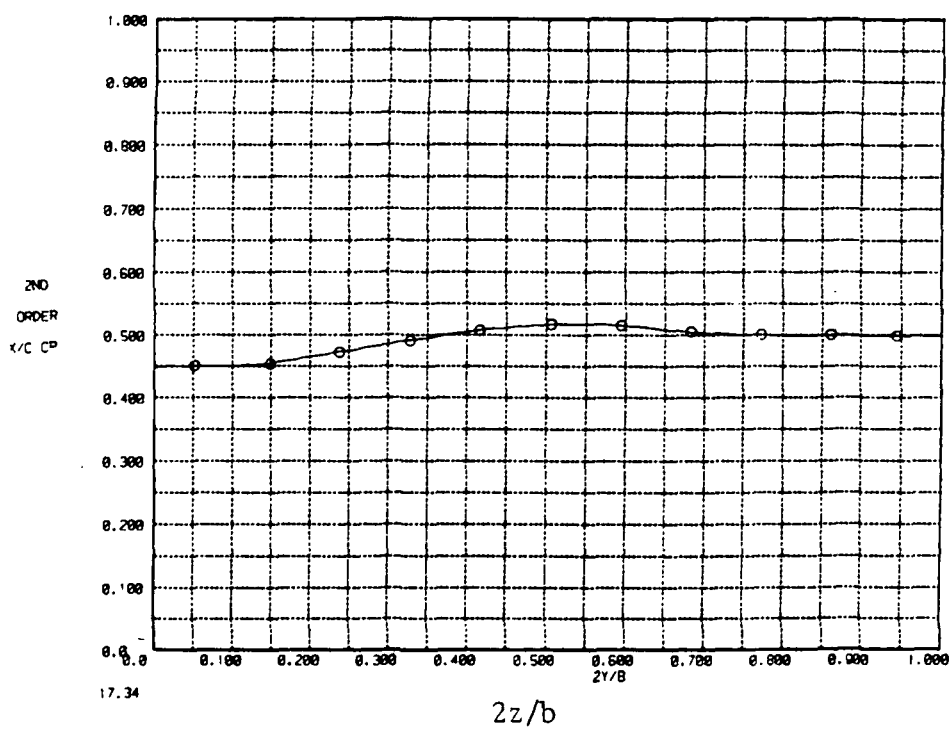

d) Sectional Center of Pressure

Figure 4.3. Concluded

5. FULL POTENTIAL ANALYSIS

The full potential equation in conservative or nonconservative form is frequently used for transonic flow analysis, where the local Mach number does not exceed approximately 1.4. If the assumptions of irrotationality and isentropicity are reasonably valid, then the full potential equation is expected to yield results comparable to Euler equations, even for supersonic/hypersonic flow fields. For conceptual design studies, where short response time is desired, the full potential methods can be an attractive substitute for expensive Euler methods and less accurate linear theory methods.

A nonlinear aerodynamic prediction technique based on the full potential equation in conservation form has been developed, during this contractual effort, for the treatment of supersonic flows. A detailed description of the method has been presented in several published papers. The most recent are enclosed in Appendix A for convenience. The first paper describes the method for the treatment of predominantly supersonic flows with regions of subsonic flow that usually occur at low supersonic Mach numbers The second paper describes the grid generation method that is used in the full potential code to treat general aircraft configurations. Since the Appendix describes the full potential method, only the material not included in the published articles will subsequently be presented.

5.1 GEOMETRY

Configuration geometry input to the full potential code is described in reference 8 and summarized briefly here. The geometry is prescribed as a set of discrete points at various axial cross-sectional locations. These input points are usually obtained from a geometry package such as GEMPAK[9] or CDS[10]. The input points are then divided into several groups or patches, and for each patch a key-point system is established. The geometry at any marching plane is then obtained by joining the appropriate key-points for each patch as shown in figure 5.1. A cubic spline fit of the key-points is used to obtain the grid point distribution (clustering) on the body surface. The physical grid between the body surface and the outer free stream boundary is then generated using an elliptic grid solver.

5.2 WAKE MODEL

The first paper of the Appendix reported the development of a wake treatment for the full potential method. This treatment has now been extended for the case of swept trailing edges. Figure 5-2 shows the schematic of a general swept trailing edge wake system. As stated in the paper, in order to treat the region behind the trailing edge, an artificial cut is created and the pressure jump, [P], across such a cut is imposed to be zero as a boundary condition. (Note the nomenclature is that used in the Appendix). This is achieved by maintaining the jump in the velocity potential, ϕ, along a K = constant line (see figure 5.2) for J = 2 to be the same as the jump in ϕ, $[\phi]$, at the trailing edge. The full potential equation is not solved at grid points on the wake cut. Instead the second derivative of ϕ with respect to the radial direction η, $\phi_{\eta\eta}$, equals zero is solved to provide $[\phi_\eta] = 0$ across the wake cut. Maintaining $[\phi]$ constant along a K line provides $[\phi_\zeta] = 0$. The combination of $[\phi_\zeta] = 0$ and $[\phi_\eta] = 0$ across the cut approximately satisfies $[P] = 0$.

ORIGINAL PAGE IS
OF POOR QUALITY

5.3 SIDESLIP

A complete analysis of an aircraft configuration must address the vehicle's performance under angle of attack (α) and sideslip (β) flight conditions. For asymmetric configurations a similar pattern exists in that the flow field is not symmetric and therefore required a solution of the entire crossflow plane. Reference 11 describes the addition of sideslip to the full potential code and the highlights are given below.

For pitch problems, only the half plane needs to be solved with the plane of symmetry boundary conditions imposed along K = 2 and (KMAX-1), as shown in Figure 5.3a. Imposing the flow conditions along K = 1 are to be the same as the ones along K = 3, the L_ξ operator results in a tridiagonal system that can be easily solved. When sideslip is present the entire cross-flow plane needs to be solved as shown in Figure 5.3b. In this case, the flow conditions along K = 1 are set to be the same as the ones along K = KMAX-2. This destroys the tridiagonal nature of the L_ξ operator. A special routine has been developed to invert a matrix of the following type.

$$L_\xi = \begin{bmatrix} \times & \times & \cdots & \cdots & \times & 0 \\ \times & \times & \times & \cdots & 0 & 0 \\ & \times & \times & \times & & \\ & & \ddots & \ddots & \ddots & \\ 0 & 0 & \cdots & \times & \times & \times \\ 0 & \times & \cdots & \cdots & \times & \times \end{bmatrix} \qquad (1)$$

In the current formulation, positive angle of attack α represents a positive Cartesian velocity v in the free stream and similarly positive sideslip β produces a positive w in the free stream. When both angle of attack and yaw are present, first the free stream is turned by an angle β and then by α. Let (x,y,z) be the inertial Cartesian system. After an initial sideslip turn β let the wind axis system be (x',y',z'), and after a subsequent α turn let it become $(\tilde{x},\tilde{y},\tilde{z})$. Then, referring to Figure 5.4

$$\begin{pmatrix} \tilde{x} \\ \tilde{y} \\ \tilde{z} \end{pmatrix} = \begin{bmatrix} \cos\alpha & \sin\alpha & 0 \\ -\sin\alpha & \cos\alpha & 0 \\ 0 & 0 & 1 \end{bmatrix} \begin{bmatrix} \cos\beta & 0 & \sin\beta \\ 0 & 1 & 0 \\ -\sin\beta & 0 & \cos\beta \end{bmatrix} \begin{pmatrix} x \\ y \\ z \end{pmatrix}$$

$$= \begin{bmatrix} \cos\alpha\cos\beta & \sin\alpha & \cos\alpha\sin\beta \\ -\sin\alpha\cos\beta & \cos\alpha & 0 \\ -\sin\beta & 0 & \cos\beta \end{bmatrix} \begin{pmatrix} x \\ y \\ z \end{pmatrix} \qquad (2)$$

The free stream is now along $\tilde{x}$. The normalized free-stream velocity potential, ϕ'_∞, is given by

$$\phi'_\infty = \frac{\phi_\infty}{U_\infty} = x \cos\alpha \cos\beta + y \sin\alpha + z \cos\alpha \sin\beta \tag{3}$$

Using equation (2), the drag, lift and side force are

$$\begin{aligned} \text{Drag} &= F_x \cos\alpha \cos\beta + F_y \sin\alpha + F_z \cos\alpha \sin\beta \\ \text{Lift} &= F_x \sin\alpha \cos\beta + F_y \cos\alpha \\ \text{Side Force} &= -F_x \sin\beta + F_z \cos\beta \end{aligned} \tag{4}$$

ORIGINAL PAGE IS
OF POOR QUALITY

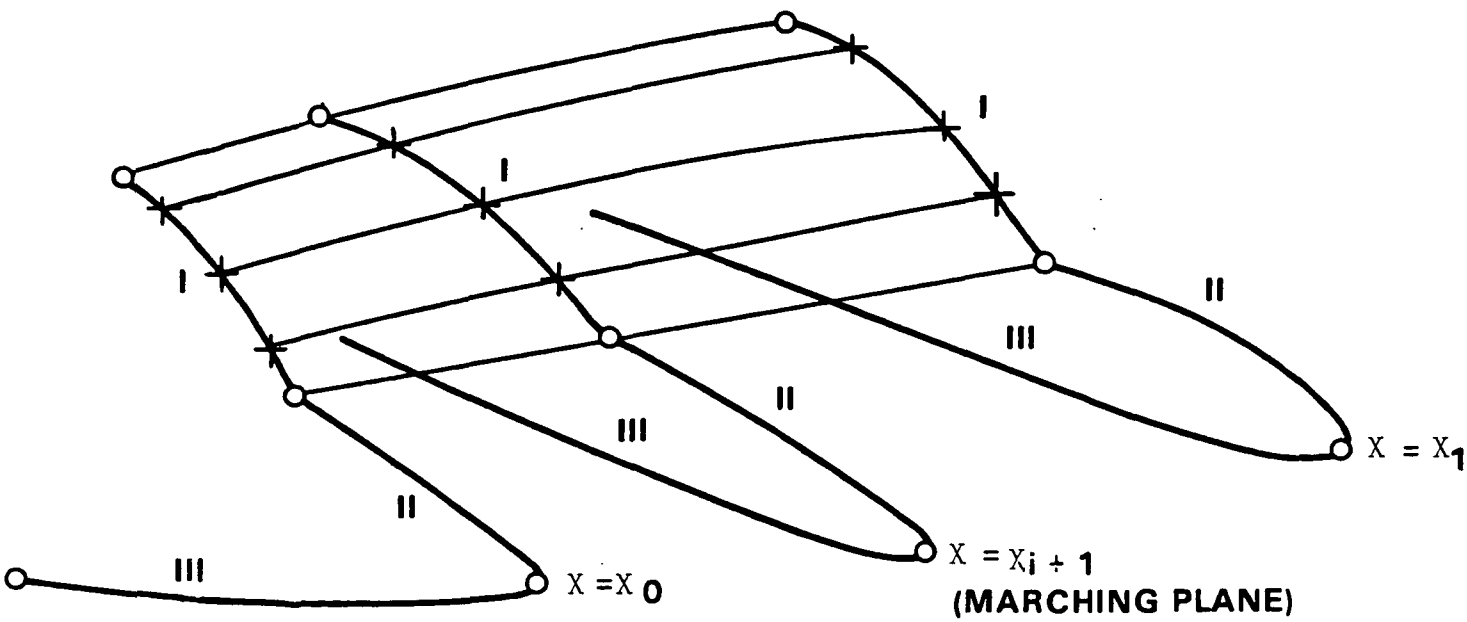

O ~ END POINTS OF A PATCH
+ ~ KEY POINTS
$X = X_0, X_1$ ~ INPUT GEOMETRY STATIONS
I, II, III, ~ PATCHES

Figure 5.1. Full Potential Geometry Input

ORIGINAL PAGE IS
OF POOR QUALITY

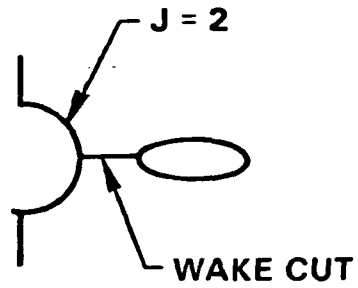

CROSS-SECTION AT
(i + 1) PLANE

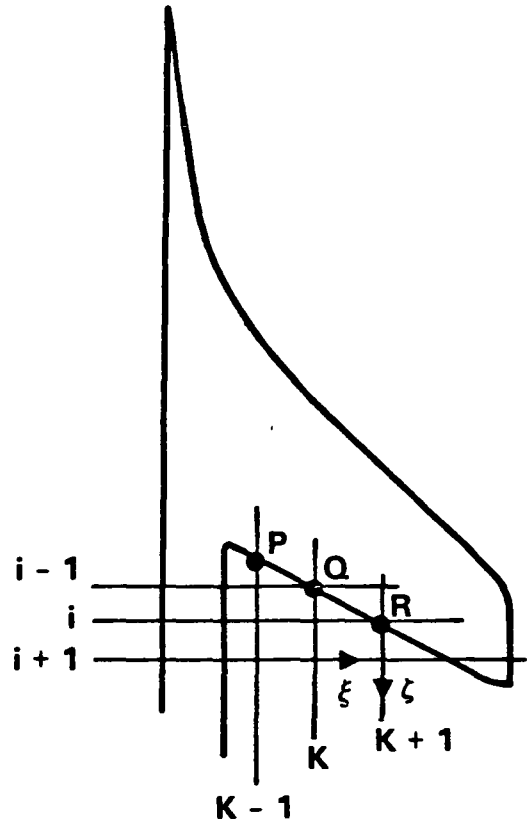

[ ] DENOTES JUMP

$[\phi]_{i+1,\,K-1} = [\phi]_P$
$[\phi]_{i+1,\,K} = [\phi]_Q$
$[\phi]_{i+1,\,K+1} = [\phi]_R$

SOLVE $\phi_{\eta\eta} = 0$ AT WAKE POINTS

Figure 5.2 Swept Trailing Edge Wake Analysis

ORIGINAL PAGE IS
OF POOR QUALITY

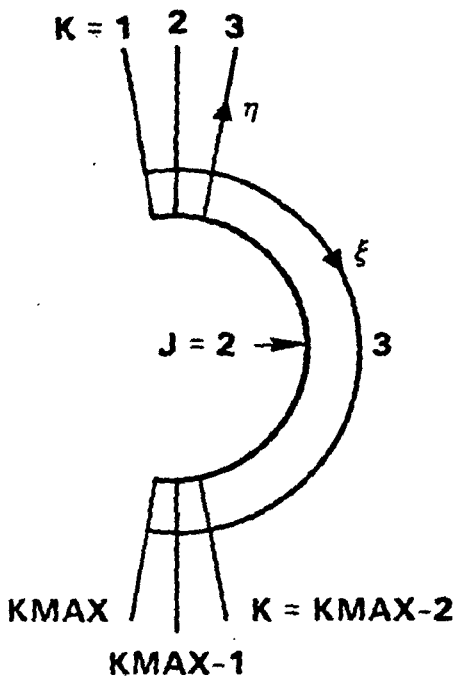

a) PLANE OF SYMMETRY

($\beta = 0$)

$\phi_{j,1} = \phi_{j,3}$

$\phi_{j,KMAX} = \phi_{j,KMAX-2}$

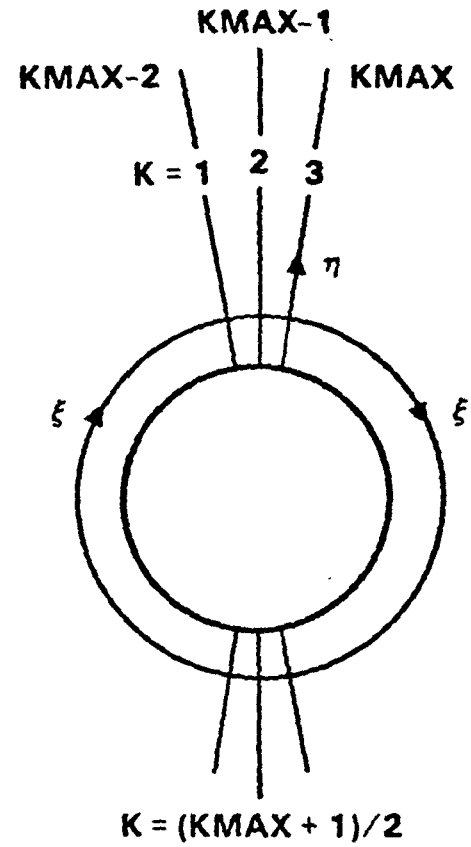

b) PERIODIC CONDITION FOR

($\beta \neq 0$)

$\phi_{j,1} = \phi_{j,KMAX-2}$

$\phi_{j,KMAX} = \phi_{j,3}$

Figure 5.3. Boundary Condition Treatment

ORIGINAL PAGE IS
OF POOR QUALITY

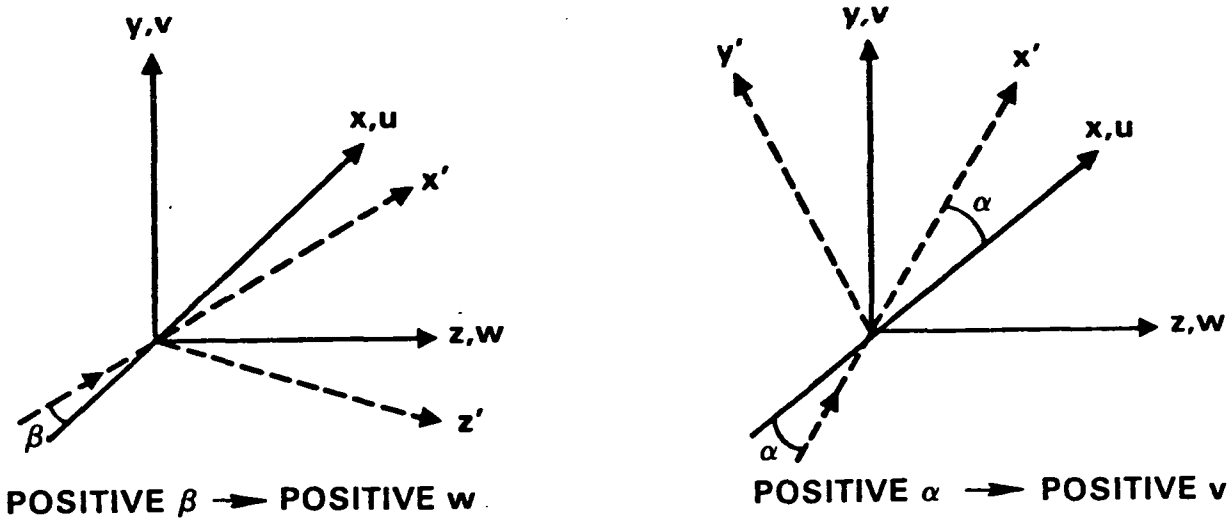

$$\begin{pmatrix} x' \\ y' \\ z' \end{pmatrix} = \begin{pmatrix} \cos\beta & 0 & \sin\beta \\ 0 & 1 & 0 \\ -\sin\beta & 0 & \cos\beta \end{pmatrix} \begin{pmatrix} x \\ y \\ z \end{pmatrix} \qquad \begin{pmatrix} x' \\ y' \\ z' \end{pmatrix} = \begin{pmatrix} \cos\alpha & \sin\alpha & 0 \\ -\sin\alpha & \cos\alpha & 0 \\ 0 & 0 & 1 \end{pmatrix} \begin{pmatrix} x \\ y \\ z \end{pmatrix}$$

Figure 5.4. Notation for Sideslip and Angle of Attack

6.0 RESULTS

6.1 SECOND ORDER

A slender delta wing-body test case[7] was initially considered for code validation purposes. The general arrangement is presented on figure 6.1.1. The wing had a leading edge sweep of seventy degrees and a maximum thickness of four percent based on sectional chord length. The body fineness ratio, ℓ/d, was twelve with a body width to wing span ratio, w/b, of twenty five percent. Experimental data and first and second order predictions covering a Mach number range of 2 to 7.4 are presented in figure 6.1.2 for lift curve slope, longitudinal stability parameter, dC_m/dC_L, and drag due to lift factor*. The experimental test results were generally linear up through maximum lift-drag ratio and consequently the previously cited aerodynamic parameters are constant in agreement with second order theory. Comparison of the estimations with measurements indicate a systematically improved correlation for second order analysis. The general prediction success is considered to be satisfactory for conceptual/preliminary design studies. Further, the analysis is responsive to such activities since a total CPU time of two minutes on an IBM 3033 was required to generate the results for the seven Mach numbers considered.

*Minimum drag was not correlated as a result of uncertainties associated with prediction of untripped experimental friction drag levels.

ORIGINAL PAGE IS
OF POOR QUALITY

$AR = 1.46$
$\lambda = 0$
$\Lambda_{LE} = 70°$
$\frac{t}{c} = .04$ 30-70 Hex Section
$\frac{d}{b} = .25$
$\frac{\ell}{d} = 12$

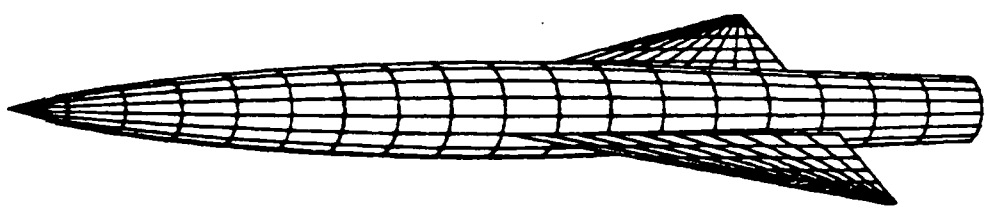

Figure 6.1.1. Delta Wing-Body Geometry

ORIGINAL PAGE IS
OF POOR QUALITY

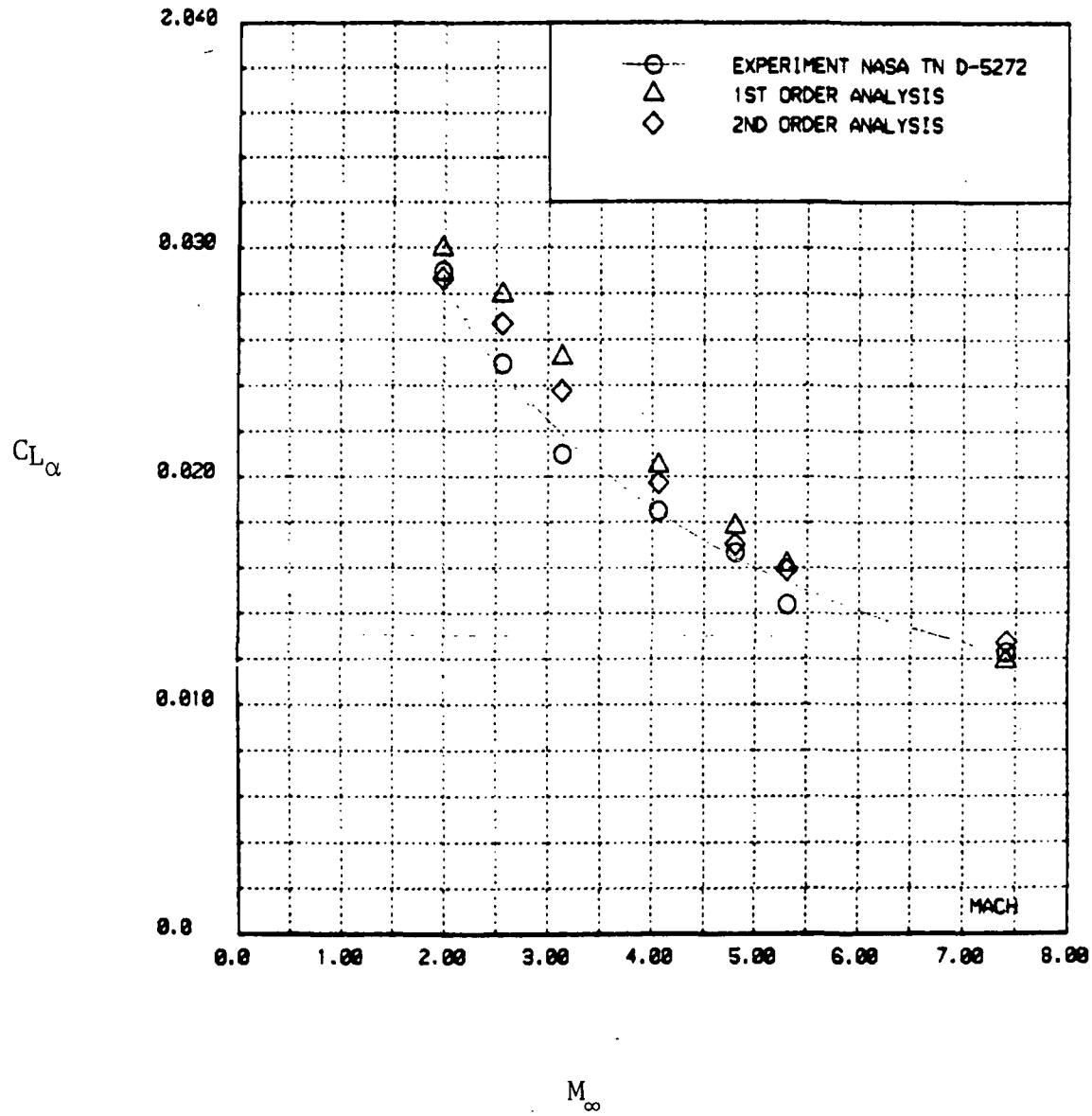

a) Lift Curve Slope

Figure 6.1.2. Delta Wing-Body Test Case

ORIGINAL PAGE IS
OF POOR QUALITY

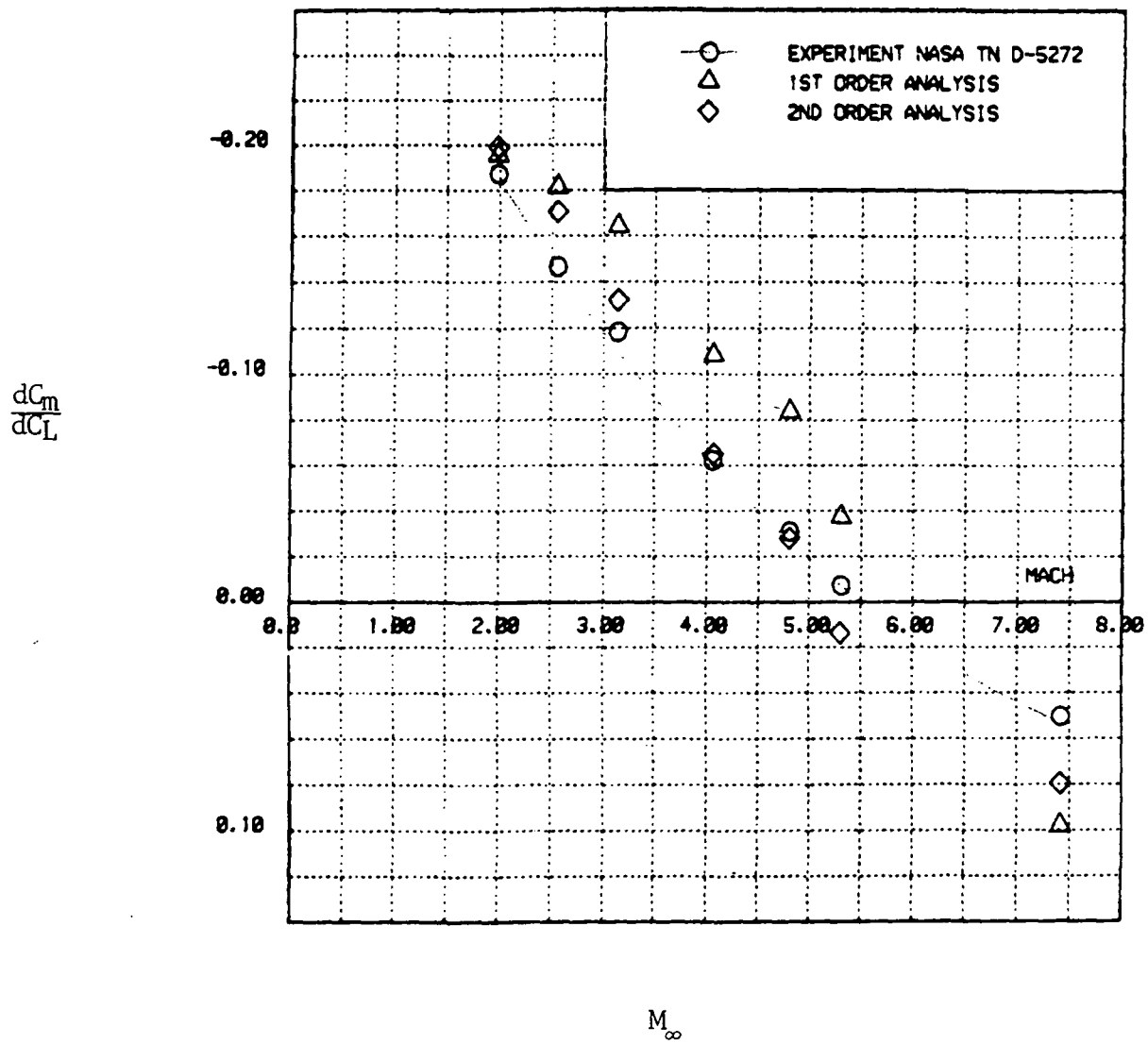

b) Longitudinal stability

Figure 6.1.2. Continued

ORIGINAL PAGE IS
OF POOR QUALITY

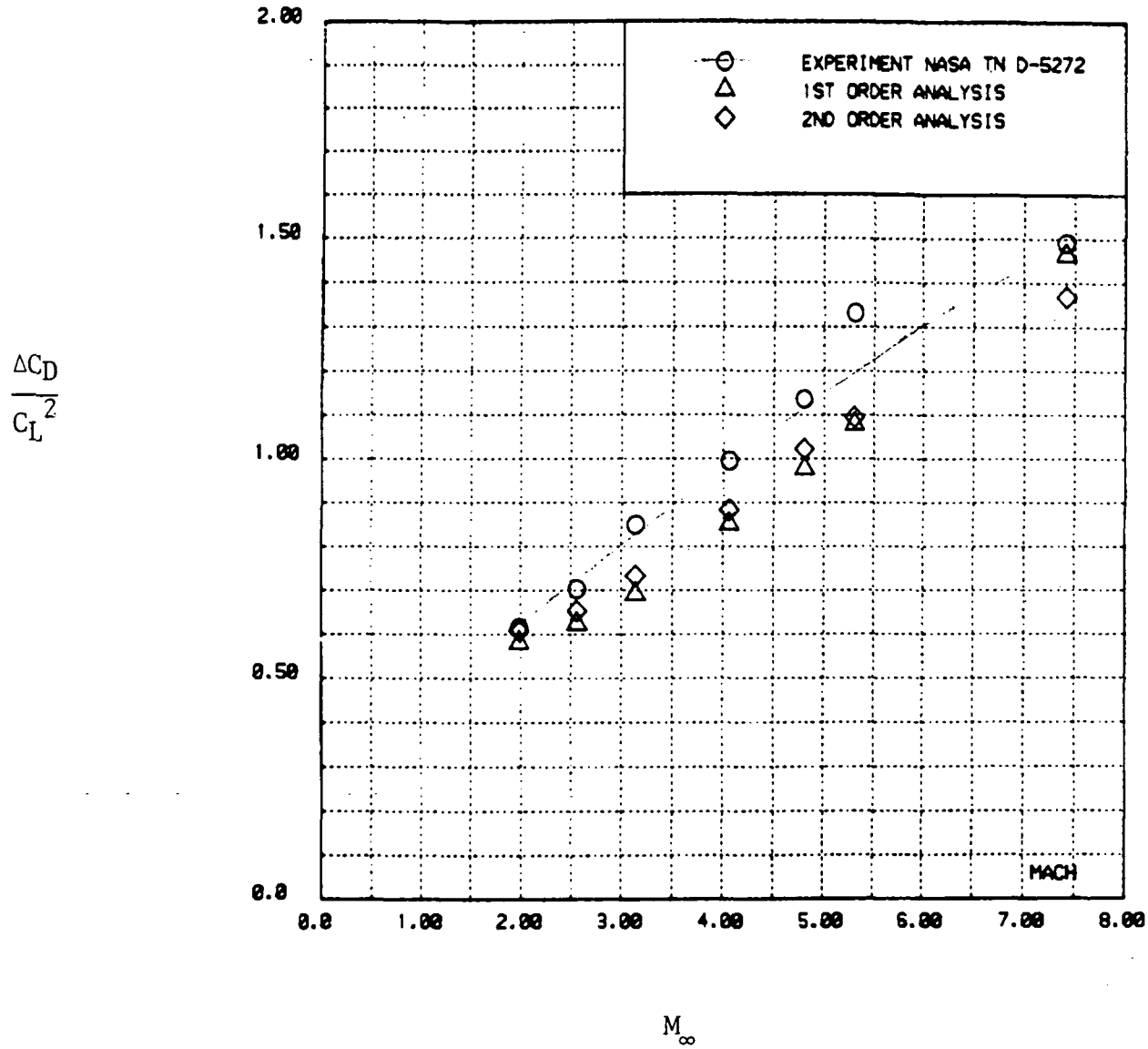

2) Drag due to lift factor

Figure 6.1.2. Concluded

6.2 FULL POTENTIAL

Figure 6.2.1 presents the pressure distribution on the surface of an arrow-wing configuration[12] at axial location $x/\ell = 0.8$ for $M_\infty = 2.98$ and $\alpha = 10.01°$. The improvement in the prediction using the wake model is illustrated. The dashed line represents the result for no wake treatment (assumes a flat plate behind the trailing edge) and the solid line shows the improvement in the pressure distribution for a zero jump in pressure across the wake cut. The solid line pressures on the body agree very well with experiments and are expected to improve force and moment calculations.

Figure 6.2.2 presents the pressure distribution on a forebody[13] at $M_\infty = 2.5$ and a sideslip $\beta = 5.02°$. The axial pressure distributions compare well with experimental data. Figure 6.2.3 shows the circumferential pressure distribution for the same forebody at $x/\ell = 0.68$ for $M_\infty = 1.7$, $\alpha = 10°$ and $\beta = 5.02°$. The comparison with experimental data is again very good.

ORIGINAL PAGE IS
OF POOR QUALITY

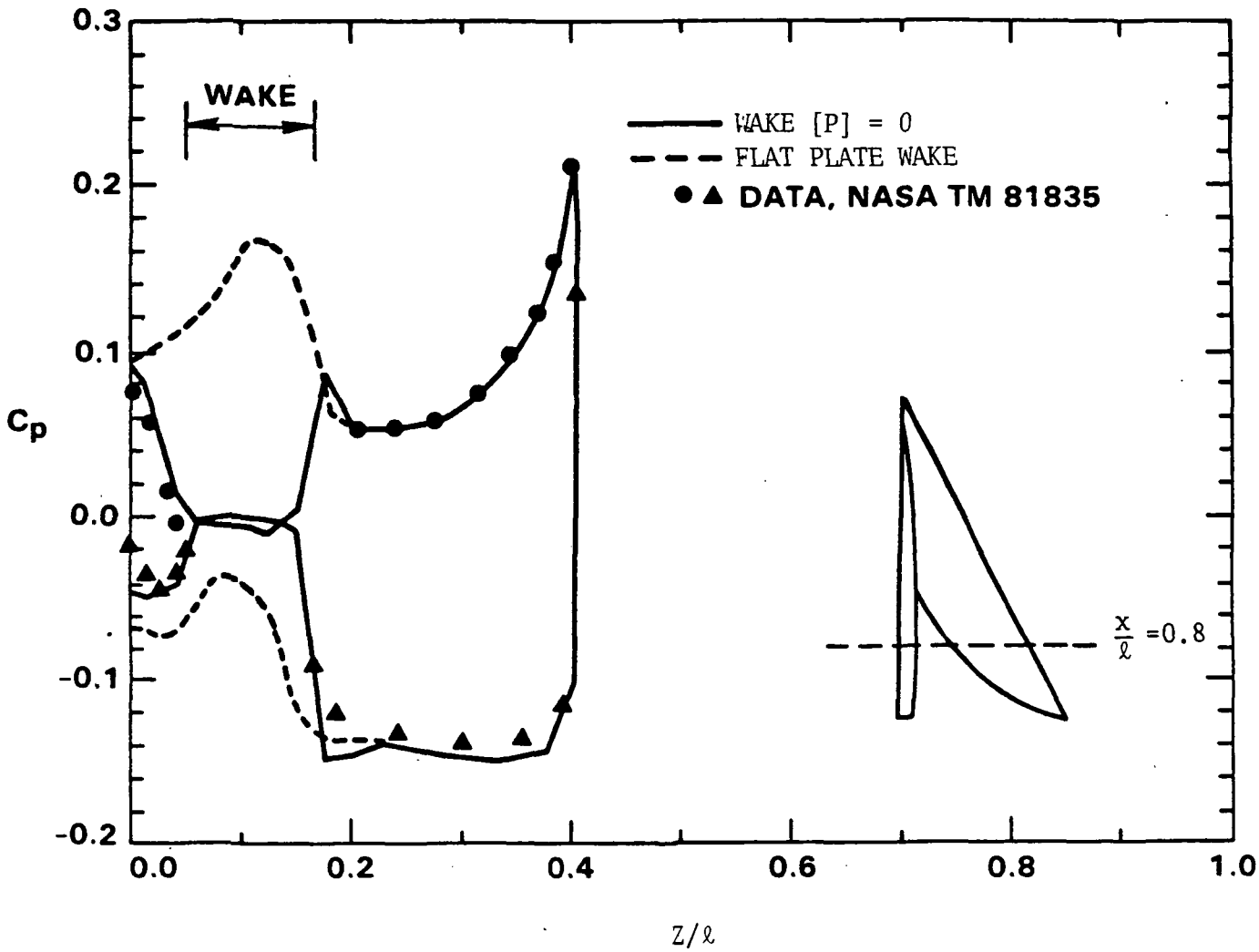

Figure 6.2.1. Pressure Distribution at $x/\ell = 0.8$ for an Arrow Wing; $M_\infty = 2.96$, $\alpha = 10.01°$

ORIGINAL PAGE IS
OF POOR QUALITY

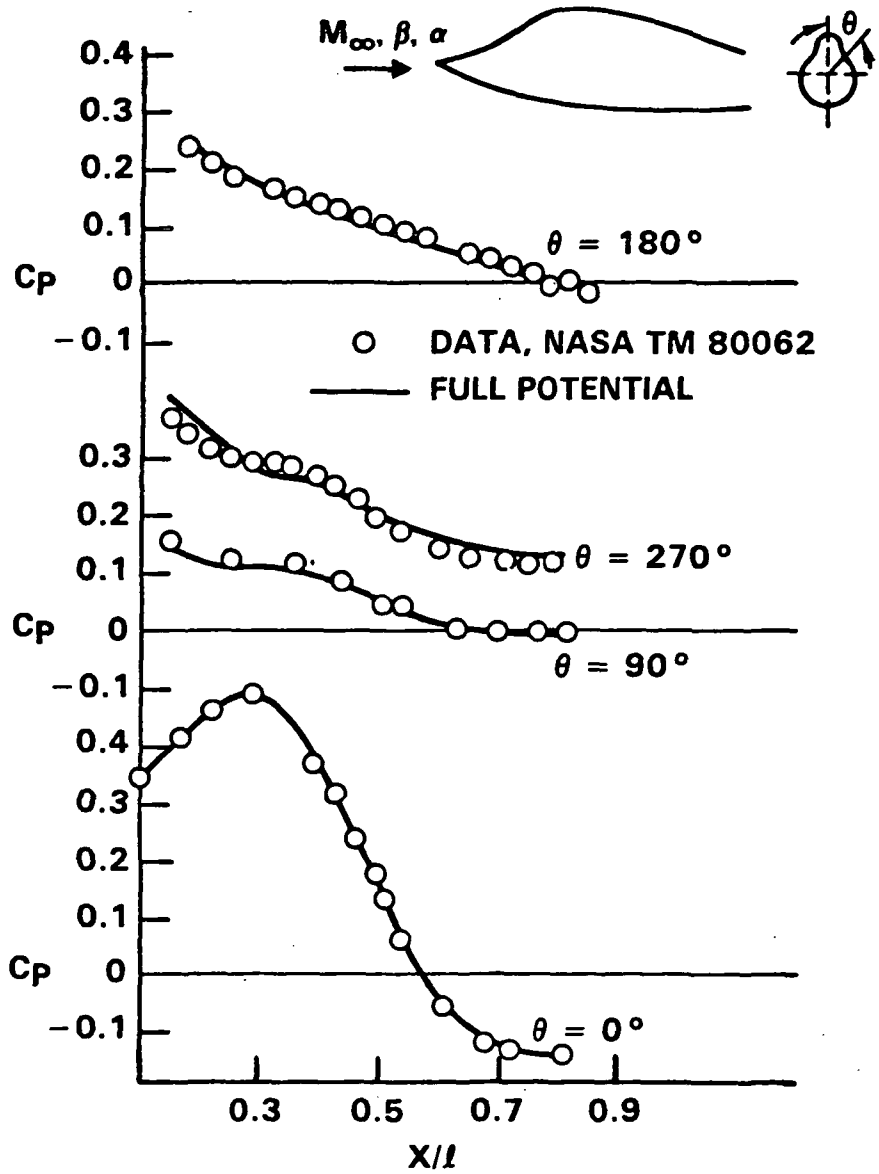

Figure 6.2.2. Pressure Distribution on a Forebody in Sideslip
$M = 2.5$, $\beta = 5.02°$, $\alpha = 0°$

ORIGINAL PAGE IS
OF POOR QUALITY

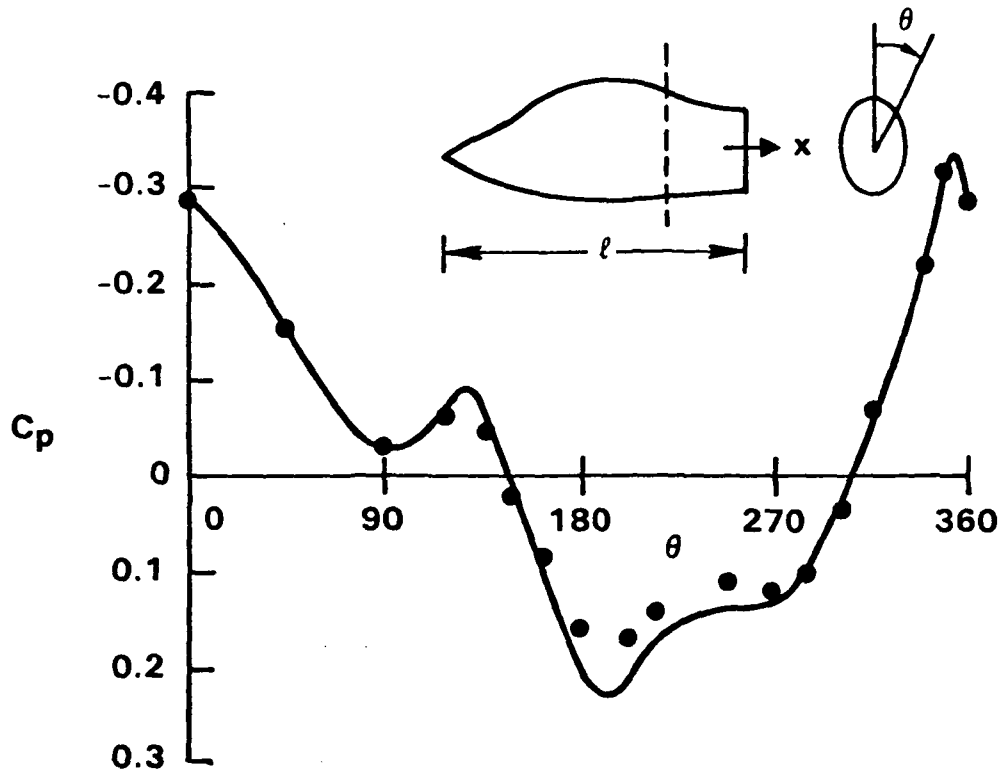

Figure 6.2.3. Circumferential Pressure Distribution at $x/\ell = 0.68$ for a Forebody in Pitch and Sideslip, $M_\infty = 1.7$, $\alpha = 10.0°$, $\beta = 5.02°$

7. CONCLUSIONS

Based on the theoretical development and comparison with experimental measurements described in this document, the following conclusions are made.

1. Improved prediction of supersonic/hypersonic aerodynamic characteristics and surface pressures for general wing-body shapes has been demonstrated using nonlinear potential analysis for values of the hypersonic similarity parameter, $M\delta$, less than one.

2. Full potential analysis successfully eliminates subsonic edge singularities and linear characteristics approximations of second order theory. The formulation is an order of magnitude faster than Euler solvers while maintaining comparable prediction accuracy for flows of moderate shock strength.

3. Nonlinear potential theory provides advanced aerodynamic prediction techniques that are responsive to the conceptual design problem at supersonic and moderate hypersonic conditions.

8. REFERENCES

1. Clever, W. C., Malmuth, N. D., and Shankar, V., "Formulation of Aerodynamic Prediction Techniques for Hypersonic Configuration Design," NASA CR-158994, February 1979.

2. Clever, W. C. and Shankar, V., "Aerodynamic Prediction Techniques for Hypersonic Configuration Design," NASA CR-165651, March 1981.

3. Clever, W. C. and Shankar, V., "Nonlinear Potential Analysis Techniques for Supersonic/Hypersonic Configuration Design," NASA CR-166078, March 1983.

4. Gunness, R. C., Knight, C. J., and Sylva, I. D., "Flow Field Analysis of Aircraft Configurations using a Numerical Solution to the Three Dimensional Unified Supersonic/Hypersonic Small-Disturbance Equations," NASA CR-1926, February 1972.

5. Bonner, E., Clever, W. C., and Dunn, K., "Aerodynamic Preliminary Analysis System II" Part I - Theory, NASA CR-165627, April 1981.

6. Divan, P., "Aerodynamic Preliminary Analysis System II," Part II - User's Manual, NASA CR-165628, April 1981.

7. Helms, W. P., and Carmichael, R. L., "An Experimental and Theoretical Investigation of a Symmetrical and a Cambered Delta Wing Configuration at Mach numbers from 2.0 to 10.7," NASA TN D-5272, June 1969.

8. Jones K. M., "Application of a Full Potential Method for Predicting Supersonic Flow Fields and Aerodynamic Characteristics," AIAA Paper No. 83-1802, presented at the AIAA Applied Aerodynamics Conference, Danvers, Massachusetts, July 1983.

9. Stack, S. H., Edwards, C. L. W., and Small, W. J., "GEMPAK: An Arbitrary Aircraft Geometry Generator," NASA TP-1022, December 1977.

10. Raymer, D. P., "Configuration Development System," Rockwell International Report TFD-78-755-4, April 1983.

11. Jones, K. M., Talcott, N. A., Jr., and Shankar V., "Application of a Full Potential Method for Computation of Three-Dimensional Supersonic Flows," AIAA Paper No. 84-0139, presented at the AIAA 22nd Aerospace Science Meeting, Reno, Nevada, January 1984.

12. Townsend, J. C., "Pressure Data for Four Analytically Defined Arrow Wings in Supersonic Flow," NASA TM 81835, September 1980.

13. Townsend, J. C., Howell, D. T., Collins, I. K., and Hayes, C., "Surface Pressure Data on a Series of Analytic Forebodies at Mach Numbers from 1.7 to 4.5 and Combined Angles of Attack and Sideslip," NASA TM 80062, June 1979.

APPENDIX A CONTRACT PUBLICATIONS

AIAA Paper No. 83-1887*

ASME Paper No. G00222

*Premission to reprint the papers appearing in this Appendix was granted by the AIAA March 6, 1984

AIAA Paper No. 83-1887

A CONSERVATIVE TYPE-DEPENDENT FULL POTENTIAL METHOD FOR THE TREATMENT OF SUPERSONIC FLOWS WITH EMBEDDED SUBSONIC REGIONS

Vijaya Shankar* and Kuo-Yen Szema**
Rockwell International Science Center
Thousand Oaks, California

and

Stanley Osher†
University of California
Los Angeles, California

ORIGINAL PAGE IS
OF POOR QUALITY

Abstract

A nonlinear method based on the full potential equation in conservation form, cast in an arbitrary coordinate system, has been developed to treat predominantly supersonic flows with embedded subsonic regions. This type of flow field occurs frequently near the fuselage-canopy junction area and wing leading edge regions for a moderately swept fighter configuration. The method uses the theory of characteristics to accurately monitor the type-dependent flow field. A conservative switching scheme is developed to transition from the supersonic marching algorithm to a subsonic relaxation procedure, and vice versa. An implicit approximate factorization scheme is employed to solve the finite-differenced equation. Results are shown for a few configurations, including a wing-body-wake realistic fighter model having embedded subsonic regions.

I. Introduction

Nonlinear aerodynamic prediction methods based on the full potential equation are used regularly for treating transonic[1,2] and supersonic[3-5] flows over realistic wing-body configurations. The transonic algorithms[1,2] are designed to treat predominantly subsonic flows with pockets of supersonic regions bounded by sonic lines and shocks. The supersonic methods[3-5] are based on a marching concept, and require the flow to remain supersonic in a given marching direction. Once the marching direction velocity becomes subsonic, the domain of dependence changes, and a pure marching scheme[3-5] will violate the rules of characteristic signal propagation. The possibility of a marching velocity becoming subsonic in a supersonic flow is great, especially for low supersonic freestream Mach number flows ($M_\infty = 1.3 \sim 1.7$) over moderately swept fighter-like configurations (sweep angle $\Lambda = 45 \sim 50°$), and over forebody shapes having a sizeable fuselage-canopy junction region. *There is a strong need to construct a supersonic marching computer program that has built-in logics to detect and treat the embedded subsonic regions.*

The method of Ref. 5 is based on the characteristic theory of signal propagation and uses a generalized, nonorthogonal, curvilinear coordinate system. Compared to other nonlinear supersonic methods[3], the method of Ref. 5 has no restrictions (limitations of the full potential theory hold) on its applicability to complex geometries and intricate shocked flow fields. It is a conservative formulation and uses numerical mapping techniques to generate the body-fitted system. The purpose of this paper is to describe an extension to the methodology of Ref. 5 to include the treatment of embedded subsonic regions in a supersonic flow.

The paper describes the characteristic theory involved in determining the condition for a marching direction to exist. Once that condition is violated, the marching scheme is transitioned to a relaxation scheme through a conservative switching operator. For marching condition violation, the total velocity q does not have to be subsonic. Even for a supersonic total velocity q, if the component in the marching direction is subsonic, a relaxation scheme is required. In order to properly produce the necessary artificial viscosity through density biasing, the paper defines two situations: one, the total velocity q is supersonic, but the marching direction component is subsonic (defined as Marching Subsonic Region (MSR) in the paper), and two, the total velocity q is subsonic (termed as Total Subsonic Region (TSR) in the paper).

Results are presented for a few configurations that exhibit either the MSR or both the MSR and TSR flow field. The paper also presents results from a wake model applied to a realistic wing-body fighter configuration.

The Appendix describes a flux biasing concept which will supersede the density biasing procedures currently in use.

The methodology of this paper is not restricted to the full potential equation alone. Currently, similar marching/relaxation methods are under development at Rockwell for application in paraboloized Navier-Stokes (PNS) codes to treat the embedded subsonic regions or streamwise separated flows without having to use a time-dependent Navier-Stokes program.

II. Equation and Characteristic Theory

The conservative full potential equation cast in an arbitrary coordinate system defined by $\zeta = \zeta(x,y,z)$, $\eta = \eta(x,y,z)$, and $\xi = \xi(x,y,z)$, takes the form

*Manager, Computational Fluid Dynamics Group, Associate Fellow AIAA

**Member Technical Staff, Member AIAA

†Professor, Department of Mathematics, Member AIAA

ORIGINAL PAGE IS
OF POOR QUALITY

$$\left(\rho \frac{U}{J}\right)_\zeta + \left(\rho \frac{V}{J}\right)_\eta + \left(\rho \frac{W}{J}\right)_\xi = 0 , \qquad (1)$$

where U, V, and W are the contravariant velocity components. Introducing the following notation for convenience

$$U = U_1 \ , \quad V = U_2 \ , \quad W = U_3$$

$$x = x_1 \ , \quad y = x_2 \ , \quad z = x_3$$

$$\zeta = X_1 \ , \quad \eta = X_2 \ , \quad \xi = X_3$$

the contravariant velocities and density are given by

$$U_i = \sum_{j=1}^{3} a_{ij}\phi_{X_j} \qquad i = 1,2,3$$

$$a_{ij} = \sum_{k=1}^{3} \frac{\partial X_i}{\partial x_k}\frac{\partial X_j}{\partial x_k} \qquad \begin{matrix} i = 1,2,3 \\ j = 1,2,3 \end{matrix} \quad \text{(transformation metrics)} \quad (2)$$

$$\rho = \left[1 - \left(\frac{\gamma-1}{2}\right) M_\infty^2 \left\{U\phi_\zeta + V\phi_\eta + W\phi_\xi - 1\right\}\right]^{1/(\gamma-1)}$$

$$a = \text{speed of sound} = \sqrt{\rho^{(\gamma-1)}/M_\infty^2} \ .$$

The Jacobian of the transformation J is represented by

$$J = \frac{\partial(\zeta,\eta,\xi)}{\partial(x,y,z)} = \begin{bmatrix} \zeta_x & \zeta_y & \zeta_z \\ \eta_x & \eta_y & \eta_z \\ \xi_x & \xi_y & \xi_z \end{bmatrix} . \qquad (3)$$

Equation (1) is in terms of a general coordinate system (ζ,η,ξ) and can accommodate any kind of mapping procedure, either analytical (conformal mapping) or numerical type. The nature of Eq. (1) can be analyzed by studying the eigenvalue system of Eq. (1). Combining the irrotationality condition in the (ζ,η) and (ζ,ξ) plane and Eq. (1), one can write the following matrix equation

$$Af_\zeta + Bf_\eta + Cf_\xi = 0 \qquad (4)$$

where

$$A = \begin{bmatrix} \frac{1}{J}(\rho U)_{\phi_\zeta} & \frac{1}{J}(\rho U)_{\phi_\eta} & \frac{1}{J}(\rho U)_{\phi_\xi} \\ 0 & 1 & 0 \\ 0 & 0 & 1 \end{bmatrix}$$

$$B = \begin{bmatrix} \frac{1}{J}(\rho V)_{\phi_\zeta} & \frac{1}{J}(\rho V)_{\phi_\eta} & \frac{1}{J}(\rho V)_{\phi_\xi} \\ -1 & 0 & 0 \\ 0 & 0 & 0 \end{bmatrix}$$

$$C = \begin{bmatrix} \frac{1}{J}(\rho W)_{\phi_\zeta} & \frac{1}{J}(\rho W)_{\phi_\eta} & \frac{1}{J}(\rho W)_{\phi_\xi} \\ 0 & 0 & 0 \\ -1 & 0 & 0 \end{bmatrix}$$

$$f = \begin{bmatrix} \phi_\zeta \\ \phi_\eta \\ \phi_\xi \end{bmatrix}$$

The subscripts in Eq. (4) denote differentiation with respect to that variable.

The matrices A, B, and C appearing in Eq. (4) can now be analyzed to determine the character of that equation. In general, the following is true:

1) Equation (4) is *elliptic in the ζ direction* if the matrix $A^{-1}(\alpha B + \beta C)$ has complex eigenvalues for all combinations of α and β such that $\alpha^2 + \beta^2 = 1$.

2) Equation (4) is *hyperbolic in the ζ direction* if $A^{-1}(\alpha B + \beta C)$ has real eigenvalues for all α and β satisfying $\alpha^2 + \beta^2 = 1$.

The eigenvalue structure of $A^{-1}(\alpha B + \beta C)$ can be obtained by setting the determinant

$$|\alpha B + \beta C - \lambda A| = 0 \quad \text{(assuming } A^{-1} \text{ exists)} \ . \qquad (5)$$

Substituting for A, B, and C from Eq. (4), the eigenvalues of Eq. (5) are given by solving the quadratic

$$-\lambda^2(\rho U)_{\phi_\zeta} + \lambda\left[\alpha(\rho V)_{\phi_\zeta} + \beta(\rho W)_{\phi_\zeta} + \alpha(\rho U)_{\phi_\eta} + \alpha(\rho U)_{\phi_\xi}\right] - \left\{\alpha^2(\rho V)_{\phi_\eta} + \beta^2(\rho W)_{\phi_\xi} + \alpha\beta\left[(\rho W)_{\phi_\eta} + (\rho V)_{\phi_\xi}\right]\right\} = 0 \ . \qquad (6)$$

Representing Eq. (6) in the form

$$\bar{A}\lambda^2 + \bar{B}\lambda + \bar{C} = 0 \ , \qquad (7)$$

the discriminant $(\bar{B}^2 - 4\bar{A}\bar{C})$ determines the character of Eq. (4):

1) If $(\bar{B}^2 - 4\bar{A}\bar{C})$ remains *positive* for all α and β satisfying $\alpha^2 + \beta^2 = 1$, then the eigenvalues of Eq. (4) are real and direction ζ is hyperbolic (marching scheme is valid).

2) If $(\bar{B}^2 - 4\bar{A}\bar{C})$ is *negative*, then the eigenvalues of Eq. (4) are complex and direction ζ is elliptic (requires a relaxation method).

To analyze when the eigenvalue solutions of Eq. (6) are real and when complex, the discriminant $(\bar{B}^2 - 4\bar{A}\bar{C})$ is rewritten in the following form (using Eq. (2))

$$\bar{B}^2 - 4\bar{A}\bar{C} = \alpha^2\left[\left(a_{21} - \frac{UV}{a^2}\right)^2 - \left(a_{11} - \frac{U^2}{a^2}\right)\left(a_{22} - \frac{V^2}{a^2}\right)\right]$$
$$+ 2\alpha\beta\left[\left(a_{21} - \frac{UV}{a^2}\right)\left(a_{31} - \frac{UW}{a^2}\right) - \left(a_{11} - \frac{U^2}{a^2}\right)\left(a_{23} - \frac{VW}{a^2}\right)\right]$$
$$+ \beta^2\left[\left(a_{31} - \frac{UW}{a^2}\right)^2 - \left(a_{11} - \frac{U^2}{a^2}\right)\left(a_{33} - \frac{W^2}{a^2}\right)\right] . \qquad (8)$$

Using the properties of a positive definite quadratic form and the Schwarz inequality ($a_{ii}a_{jj} > a_{ij}^2$), Eq. (8) can be shown to have the following results:

1) $(\bar{B}^2 - 4\bar{A}\bar{C})$ is positive if $\left(a_{11} - \frac{U^2}{a^2}\right)$ is less than zero. Then the ζ direction is hyperbolic (the marching algorithm of Ref. 5 is valid).

2) $(\bar{B}^2 - 4\bar{A}\bar{C})$ is negative if $\left(a_{11} - \frac{U^2}{a^2}\right)$ is greater than zero. Then the ζ direction is elliptic (requires a relaxation scheme).

A. Physical Interpretation

The physical interpretation of these results from the characteristic theory is illustrated in Fig. 1. Let q be the total velocity. The projection of q in the direction normal to the ζ=constant surface is given by

$$\left.\begin{aligned} \vec{q}\cdot\vec{n} &= (u\hat{i} + v\hat{j} + w\hat{k})\ \frac{(\zeta_x\hat{i} + \zeta_y\hat{j} + \zeta_z\hat{k})}{\zeta_x^2 + \zeta_y^2 + \zeta_z^2} \\ &= \frac{U}{\sqrt{a_{11}}} , \end{aligned}\right\} \qquad (9)$$

where u, v, and w are the Cartesian velocities and $\vec{n}$ is the normal to the ζ=constant plane. Figure 1a shows the case when $\frac{U}{\sqrt{a_{11}}}$ is greater than the speed of sound $\left(\left(a_{11} - \frac{U^2}{a^2}\right) < 0\right)$. For this case, the characteristic cone of influence is behind the ζ=constant plane and marching along ζ is valid. Figure 1b illustrates the case for the q > a, but $\frac{U}{\sqrt{a_{11}}} < a$ situation $\left(\left(a_{11} - \frac{U^2}{a^2}\right) > 0\right)$. For this case, a part of the characteristic cone of influence lies forward of the ζ=constant plane and marching along ζ is not possible. This case (Fig. 1b) is termed Marching Subsonic Region (MSR) in this paper. Figure 1c shows the case when q < a and $\frac{U}{\sqrt{a_{11}}} < a$ $\left(\left(a_{11} - \frac{U^2}{a^2}\right) > 0\right)$. This represents a pure subsonic flow and marching along ζ is not possible. This case is termed Total Subsonic Region (TSR). For cases represented in Figs. 1b and 1c, a relaxation algorithm is required.

ORIGINAL PAGE IS
OF POOR QUALITY

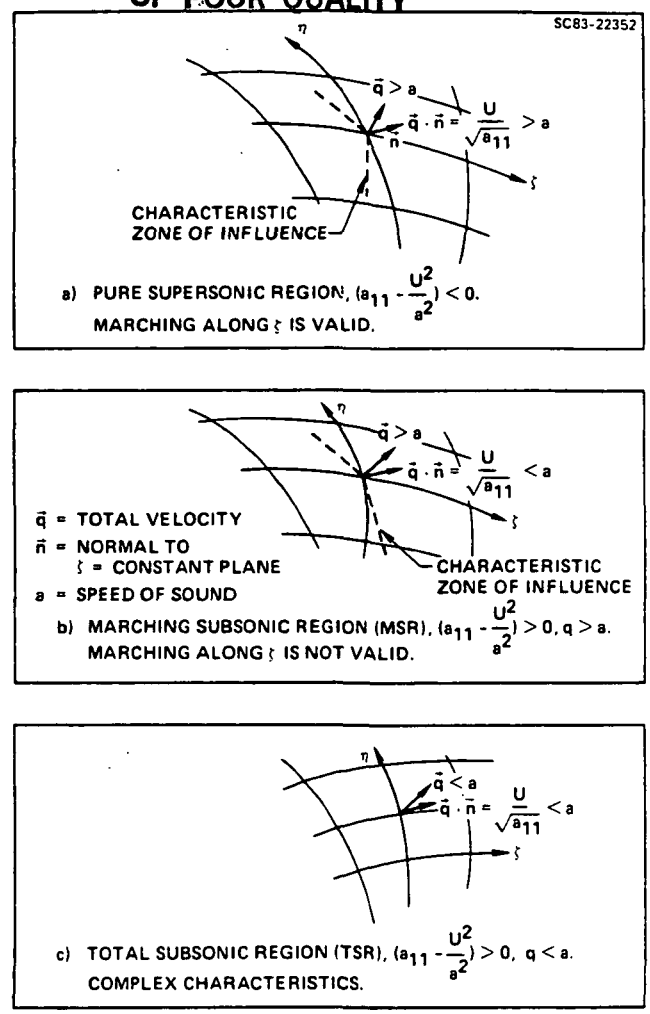

Fig. 1. Role of characteristics in defining supersonic region, Marching Subsonic Region (MSR), and Total Subsonic Region (TSR).

III. Numerical Method

Figure 2 shows the schematic of a fuselage-canopy forebody geometry with an embedded MSR and TSR present in a supersonic flow. To solve this problem, the marching scheme of Ref. 5 will be used when $\left(a_{11} - \frac{U^2}{a^2}\right)$ is negative, and a relaxation scheme

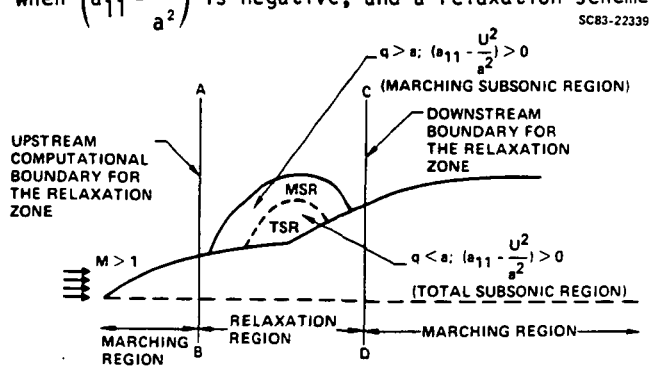

Fig. 2. Embedded subsonic bubble in a supersonic flow.

ORIGINAL PAGE IS
OF POOR QUALITY

when $\left(a_{11} - \frac{U^2}{a^2}\right)$ is positive. First, march from the nose up to the plane denoted by (A-B) in Fig. 2, using the method of Ref. 5. Then, between (A-B) and (C-D), which embed the subsonic bubble (MSR and TSR), use a relaxation scheme and iterate until the subsonic bubble is fully captured. Then, resume the marching scheme from the plane (C-D), downstream of the body.

The purpose of this paper is to present a conservative algorithm that will automatically switch from a pure marching scheme of Ref. 5 to a relaxation method at the onset of an MSR formation and revert to the marching procedure when the flow becomes fully supersonic again. The entire flow field can be classified into three types with respect to the marching direction ζ:

1) At a grid point, the marching direction is *hyperbolic* and the total velocity q is supersonic, $\left(a_{11} - \frac{U^2}{a^2}\right) < 0$, $q > a$. This point will use the algorithm of Ref. 5.

2) At a grid point, the marching direction ζ is *elliptic*, $\left(a_{11} - \frac{U^2}{a^2}\right) > 0$, but the total velocity q is supersonic, $q > a$ (MSR). This point will be treated by a transonic operator with a built-in density biasing based on the magnitude of $\left(1 - \frac{a^2}{q^2}\right)$.

3) At a grid point, the direction ζ is *elliptic* and the total velocity q is *subsonic*, $q < a$ (TSR). This point will be treated by a subsonic central differenced operator.

A. Treatment of $\frac{\partial}{\partial\zeta}\left(\rho \frac{U}{J}\right)$ in Eq. (1)

Refer to the computational molecule in Fig. 3.

$$\frac{\partial}{\partial\zeta}\left(\rho \frac{U}{J}\right) = \theta_i \underbrace{\overleftarrow{\partial}_\zeta \left(\rho \frac{U}{J}\right)_{i+1}}_{\text{supersonic}} + (1 - \theta_{i+1}) \underbrace{\overrightarrow{\partial}_\zeta \left(\tilde{\rho} \frac{U}{J}\right)_{i+1}}_{\text{marching subsonic}} \tag{10}$$

where

$\overleftarrow{\partial}$ refers to backward differencing

$\overrightarrow{\partial}$ refers to forward differencing

$$\theta_i = 1 \quad \text{if} \quad \left(a_{11} - \frac{U^2}{a^2}\right) < 0$$

$$= 0 \quad \text{if} \quad \left(a_{11} - \frac{U^2}{a^2}\right) > 0 \ .$$

In Eq. (10), the first term corresponds to the supersonic marching operator of Ref. 5, and the second term is the subsonic operator.

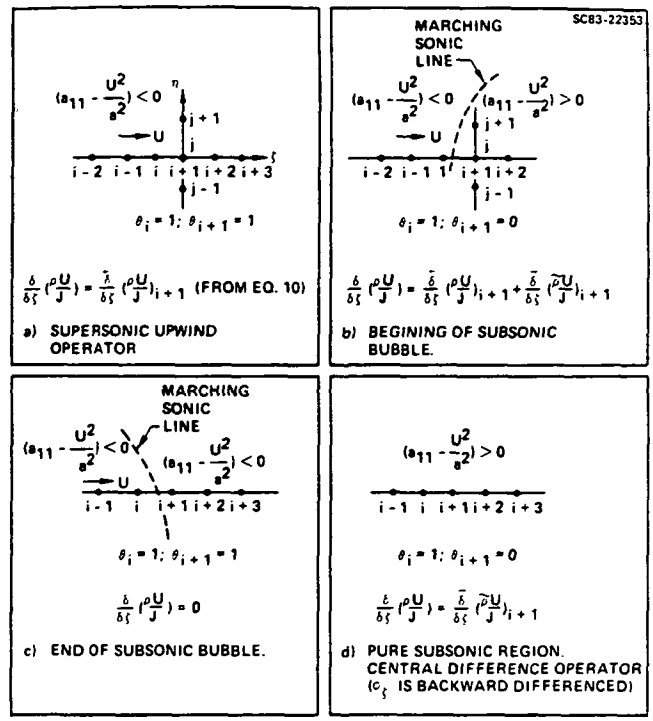

Fig. 3. Conservative type-dependent switching scheme for the treatment of subsonic bubble in a supersonic flow.

The backward difference operator in Eq. (10) is represented by

$$\overleftarrow{\partial}_\zeta \left(\rho \frac{U}{J}\right)_{i+1} \doteq \overleftarrow{\partial}_\zeta \rho_i \left[\left(a_{11} - \frac{U^2}{a^2}\right) \overleftarrow{\partial}_\zeta \Delta\phi + \left(a_{12} - \frac{UV}{a^2}\right) \frac{\partial}{\partial\eta} \Delta\phi + \left(a_{13} - \frac{UW}{a^2}\right) \frac{\partial}{\partial\xi} \Delta\phi + U_i\right] , \tag{11}$$

$$\Delta\phi = (\phi_{i+1} - \phi_i) \ .$$

The term $\frac{\partial}{\partial\zeta}(\Delta\phi)$ is backward differenced. Reference 5 gives more details on this supersonic marching operator.

The forward difference operator in Eq. (10) is represented by

$$\overrightarrow{\partial}_\zeta \left(\tilde{\rho} \frac{U}{J}\right)_{i+1} \doteq \overrightarrow{\partial}_\zeta \left[\frac{\tilde{\rho}^{n+1}_{i+1}}{J} \left(a_{11}\overleftarrow{\phi}_\zeta + a_{12}\phi_\eta + a_{13}\phi_\xi\right)_{i+1}\right] \tag{12}$$

where

$$\tilde{\rho}^{n+1}_{i+1} = \rho^n_{i+1} - \nu(\rho^n_{i+1} - \rho^n_i) \ , \ \text{for } U > 0$$

$$\nu = \max\left(0, 1 - \frac{a^2}{q^2}\right) \ . \tag{13}$$

ORIGINAL PAGE IS
OF POOR QUALITY

The superscript n+1 denotes the current relaxation cycle for a subsonic bubble calculation.

Note that in Eq. (12) the term ϕ_ζ is backward differenced such that $\frac{\overleftarrow{\partial}}{\partial\zeta}\frac{\tilde{\rho}}{J}a_{11}\overleftarrow{\phi}_\zeta$ will provide the central differencing needed for an elliptic (subsonic) point. The density biasing, Eq. (13), is activated only when the total velocity q is greater than the speed of sound a. This will take place when a grid point is in the region denoted by MSR in Fig. 2. When q < a, region TSR in Fig. 2, the density is not biased and the generation of artificial viscosity is turned off. The ϕ derivatives in Eq. (13) can be rewritten in terms of $\Delta\phi$, just like in Eq. (11).

Equation (10) can also be interpreted as

$$\frac{\partial}{\partial\zeta}\left(\rho\frac{U}{J}\right) = \underbrace{\frac{\overleftarrow{\partial}}{\partial\zeta}\left(\rho\frac{U}{J}\right)_{i+1}}_{\text{elliptic operator}} \underbrace{- \Delta\zeta\frac{\overleftarrow{\partial}}{\partial\zeta}\theta_{i+1}\frac{\overleftarrow{\partial}}{\partial\zeta}\left(\rho\frac{U}{J}\right)_{i+2}}_{\text{flux biasing to produce the artificial viscosity}} . \qquad (14)$$

Figure 3 illustrates various possibilities that can be handled by Eq. (10). It has both the shock point operator and the sonic operator required to treat the type-dependent flow. The only issue that philosophically affects the concept of a conservative scheme is that the definition of ρU for a supersonic operator in Eq. (11) is different from the definition for the subsonic operator of Eq. (12).

The evaluation of the subsonic operator in Eq. (12) requires velocity potential (ϕ) values at i+1 and i+2 planes from the previous (n) relaxation cycle to compute the density. The Initial and Boundary Conditions section of this paper prescribes a method to start the first relaxation cycle of the subsonic bubble calculation.

B. Treatment of $\frac{\partial}{\partial\eta}\left(\rho\frac{V}{J}\right)$ in Eq. (1)

Referring to the Fig. 3a molecule,

$$\frac{\partial}{\partial\eta}\left(\rho\frac{V}{J}\right) = \theta_{i+1}\underbrace{\frac{\overleftarrow{\partial}}{\partial\eta}\left(\bar{\rho}\frac{V}{J}\right)_{j+\frac{1}{2}}}_{\text{supersonic}} + (1-\theta_{i+1})\underbrace{\frac{\overleftarrow{\partial}}{\partial\eta}\left(\tilde{\tilde{\rho}}\frac{V}{J}\right)_{j+\frac{1}{2}}}_{\text{marching subsonic}}$$

where

$$\theta_{i+1} = 1 \quad \text{if} \quad \left(a_{11} - \frac{U^2}{a^2}\right)_{i+1} < 0 \quad \text{(supersonic point)}$$

$$\theta_{i+1} = 0 \quad \text{if} \quad \left(a_{11} - \frac{U^2}{a^2}\right)_{i+1} \geq 0 \quad \text{(MSR)} .$$

When $\theta_{i+1} = 1$, that is, the point is *supersonic* with respect to ζ, only the first term in Eq. (15) is used and the biased density $\bar{\rho}$ is defined by (for V > 0)

$$\bar{\rho}_{j+\frac{1}{2}} = (1-\bar{\nu}_{j+\frac{1}{2}})\rho^*_{j+\frac{1}{2}} + \frac{1}{2}\bar{\nu}_{j+\frac{1}{2}}(\rho^*_j + \rho^*_{j-1}) \qquad (16)$$

where

$$\bar{\nu} = \max\left(0,\ 1 - a_{22}\frac{a^2}{V^2}\right) .$$

In Eq. (16), the evaluation of ρ^* depends on whether the flow is conical or nonconical. For conical flows, all ρ^* quantities are evaluated at the ith plane. For nonconical flows, at each nonconical marching plane, initially ρ^* is set to be the value at the ith plane and then subsequently iterated to convergence by setting ρ^* to the previous iterated value of ρ at the current i+1 plane. Reference 5 provides more details on the density biasing procedure and the implicit treatment of $\frac{\overleftarrow{\partial}}{\partial\eta}\left(\bar{\rho}\frac{V}{J}\right)_{j+\frac{1}{2}}$ in Eq. (15).

When the point is *elliptic*, the density biasing is defined by

$$\tilde{\tilde{\rho}}^{n+1}_{j+\frac{1}{2}} = (1-\tilde{\tilde{\nu}}_{j+\frac{1}{2}})\rho^n_{j+\frac{1}{2}} + \frac{1}{2}\tilde{\tilde{\nu}}_{j+\frac{1}{2}}(\rho^n_j + \rho^n_{j-1}) \qquad (17)$$

where $\tilde{\tilde{\nu}} = \max\left(0,\ 1 - \frac{a^2}{q^2}\right)$. As before, the superscript n+1 denotes the current relaxation cycle for a subsonic bubble calculation. Note the difference in the definition of $\bar{\nu}$ and $\tilde{\tilde{\nu}}$. The density biasing in the cross flow direction η is turned off when the total velocity q is less than the speed of sound a, just as in the marching ζ direction (Eq. (13)). The implicit treatment of V in the marching subsonic operator of Eq. (15) is the same as that of the supersonic part, explained in Ref. 5.

A similar procedure is implemented for the $\left(\rho\frac{W}{J}\right)_\xi$ term in Eq. (1).

D. Implicit Factorization Algorithm

Combining the various terms of Eq. (1) as represented by Eqs. (10)-(17) together with the terms arising from $\left(\rho\frac{W}{J}\right)_\xi$ will result in a fully implicit model. This is solved using an approximate factorization implicit scheme. After some rearrangement of the terms, the factored implicit scheme becomes

$$\left[1+\frac{A_3}{\beta\Delta\zeta}\frac{\partial}{\partial\xi}+\frac{1}{\beta}\frac{\partial}{\partial\xi}\left(\frac{\hat{\rho}}{J}\frac{a_{31}}{\Delta\zeta}\right)+\frac{1}{\beta}\frac{\partial}{\partial\xi}\frac{\hat{\rho}a_{33}}{J}\frac{\partial}{\partial\xi}\right]$$

$$\times\left[1+\frac{A_2}{\beta\Delta\zeta}\frac{\partial}{\partial\eta}+\frac{1}{\beta}\frac{\partial}{\partial\eta}\left(\frac{\hat{\rho}a_{21}}{J\Delta\zeta}\right)\right.$$

$$\left.+\frac{1}{\beta}\frac{\partial}{\partial\eta}\frac{\hat{\rho}a_{22}}{J}\frac{\partial}{\partial\eta}\right]\Delta\phi = R\ . \tag{18}$$

The density $\hat{\rho}$ appearing in Eq. (18) can be either $\bar{\rho}$ or $\tilde{\tilde{\rho}}$ depending on the sign of $\left(a_{11}-\frac{U^2}{a^2}\right)$ as illustrated in Eq. (15).

Equation (18) has the form

$$L_\xi L_\eta(\Delta\phi) = R \tag{19}$$

and it is implemented as follows:

$$L_\xi(\Delta\phi)^* = R \qquad L_\eta(\Delta\phi) = (\Delta\phi)^* \qquad \phi_{i+1} = \phi_i + \Delta\phi\ . \tag{20}$$

The various quantities appearing in Eq. (18) are given by

$$\beta = \frac{1}{\Delta\zeta}\left[\theta_i A_1 - (1-\theta_{i+1})\frac{\Delta\zeta}{\Delta\zeta_0}\left(\frac{\tilde{\rho}a_{11}}{J}\right)_{i+1}\right]$$

$$A_1 = \frac{\rho_i}{J_{i+1}}\left(a_{11}-\frac{U^2}{a^2}\right)$$

$$A_2 = \theta_i\left[\frac{\rho_i}{J_{i+1}}\left(a_{12}-\frac{UV}{a^2}\right)\right] - (1-\theta_{i+1})\frac{\Delta\zeta}{\Delta\zeta_0}\left(\frac{\tilde{\rho}a_{12}}{J}\right)_{i+1}$$

$$A_3 = \theta_i\left[\frac{\rho_i}{J_{i+1}}\left(a_{13}-\frac{UW}{a^2}\right)\right] - (1-\theta_{i+1})\frac{\Delta\zeta}{\Delta\zeta_0}\left(\frac{\tilde{\rho}a_{13}}{J}\right)_{i+1}$$

$$\Delta\zeta_0 = \zeta_{i+2} - \zeta_{i+1}$$

$$\Delta\zeta = \zeta_{i+1} - \zeta_i \tag{21}$$

and the right-hand side term R consists of various known quantities.

If the flow field does not contain an embedded MSR or TSR, the implicit factored algorithm of Eq. (18) performs a pure marching procedure starting from an initial known data plane. In this situation, there is no need to go back to the upstream starting plane and iterate the solution. However, if a subsonic bubble is present (between planes AB and CD in Fig. 2), then the solution procedure of Eq. (18) performs a relaxation method, and iterates for the elliptic subsonic bubble to converge (superscript n in Eqs. (12), (13), and (17) refers to the relaxation cycle counter).

E. Initial and Boundary Conditions

Initial Conditions

For a pure supersonic flow, initial conditions need to be prescribed only at the starting plane. Usually, the starting plane is set close to the apex of the configuration solved for, and conical solutions are prescribed.

Inside an MSR, as in Fig. 2, when Eq. (12) is applied at an (i+1) grid point, information on ϕ_{i+2} is required to form the density $\tilde{\rho}$ and various derivative terms. For the first relaxation pass, an initial estimate for quantities in the (i+2) plane is prescribed in the following manner:

$$\underbrace{\frac{\partial}{\partial\zeta}\left(\rho\frac{U}{J}\right)_{i+1}}_{\text{MSR operator}} = \Delta\zeta\left\{\underbrace{\left(\rho\frac{U}{J}\right)_{i+2}}_{\text{needs initial estimate}} - \left(\frac{\rho}{J}\left(a_{11}\phi_\zeta + a_{12}\phi_\eta + a_{13}\phi_\xi\right)\right)_{i+1}\right\} \tag{22}$$

In Eq. (22), sonic conditions are assumed at (i+2) for the first relaxation pass:

$$\left.\begin{aligned}\rho_{i+2} &= \rho^* \\ U_{i+2} &= q^*(a_{11})_{i+2}\end{aligned}\right\}. \tag{23}$$

The sonic values ρ^* and q^* are purely a function of the freestream Mach number M_∞. Also, ρ_{i+1} in Eq. (22) is initialized to be ρ_i.

For the second relaxation cycle and onwards ($n \geq 1$), the conditions from the previous relaxation cycle are used:

$$\left.\begin{aligned}\left(\rho\frac{U}{J}\right)^{n+1}_{i+2} &\doteq \left(\rho\frac{U}{J}\right)^{n}_{i+2} \\ \rho^{n+1}_{i+1} &\doteq \rho^{n}_{i+1}\end{aligned}\right\}\ . \tag{24}$$

Boundary Conditions

At a solid boundary, the contravariant velocity V is set to zero. Exact implementation of V = 0 in the implicit treatment of Eq. (18) is described in Ref. 4.

The outer boundary is set away from the bow shock and the freestream velocity potential ϕ_∞ is imposed along that boundary. All discontinuities in the flow field are captured. The precise density biasing activator ν, based on the characteristic theory, allows for sharp capturing of shocks in the flow.

Behind the trailing edge of a wing, a wake model is imposed. Figure 4 shows a schematic of a wake model. At a point P lying on the wake, the boundary condition is that there is no jump in the pressure across the wake, i.e., $(p_P - p_Q) = 0$. In the full potential (isentropic) formulation, this translates into the condition that the jump in density $(\rho_P - \rho_Q)$ is zero, or the jump in the total velocity q is zero ($(q_P - q_Q) = 0$). The jump in q across the wake is set to zero in an approximate manner in the following way.

First, compute the jump in the potential ϕ at the trailing edge point P', and maintain that jump

ORIGINAL PAGE IS
OF POOR QUALITY

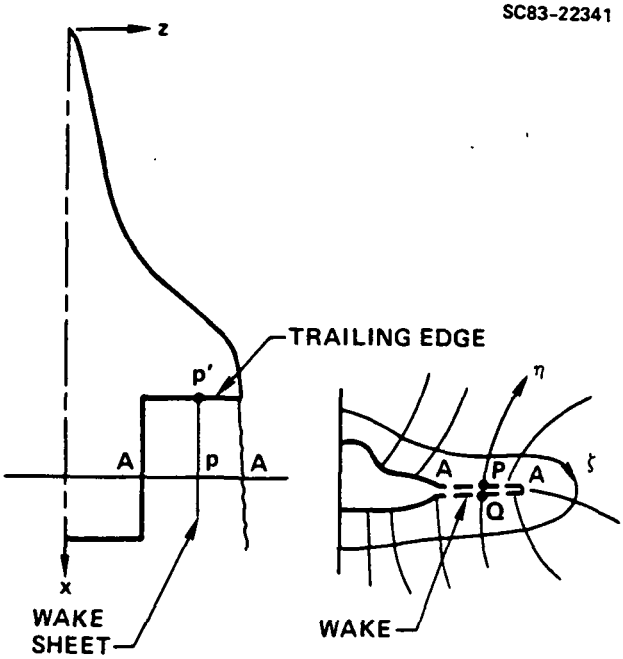

WAKE MODEL

$\phi_P - \phi_Q = \phi_{P'} - \phi_{Q'}$ (JUMP IN ϕ)

$(\phi_\zeta)_P - (\phi_\zeta)_Q \doteq 0$

$(\phi_\eta)_P - (\phi_\eta)_Q \doteq 0 \rightarrow (\phi_{\eta\eta})_P = 0$

Fig. 4. Wake boundary condition.

constant along the line P'P in Fig. 4. At the wake point P, Eq. (1) is not valid. Instead of solving Eq. (1), $\phi_{\eta\eta} = 0$ is satisfied at the wake point P, to achieve the condition $(\phi_\eta)_P - (\phi_\eta)_Q = 0$. Incorporating a constant jump in ϕ along P'P ensures $(\phi_\zeta)_P - (\phi_\zeta)_Q = 0$. The net effect is that $(q_P - q_Q)$ is approximately set to zero, yielding the necessary wake boundary condition. The Results section in this paper presents a calculation performed for a realistic wing-body-wake fighter model and shows an excellent matching of the pressures across the wake, using the above wake boundary condition.

F. Grid System

The transformation from the physical space (x,y,z) to a body-fitted computational space (ζ,η,ξ) is performed numerically at each constant ζ plane by using the elliptic grid generation technique of Ref. 6. Once the grid is generated, all the metric terms a_{ij} in Eq. (2) and the Jacobian J in Eq. (3) are computed by numerical differentiation. As described in Ref. 5, a free-stream error subtraction is performed at each grid point to account for any improper metric cancellation.

G. Density Biasing Summary

This section summarizes in a tabular form the type-dependent density biasing procedures incorporated in this paper to generate the proper artificial viscosity.

Term	Total Supersonic $\left(a_{11}-\frac{U^2}{a^2}\right)<0$, $q>a$	Marching Subsonic $\left(a_{11}-\frac{U^2}{a^2}\right)>0$, $q>a$	Total Subsonic $\left(a_{11}-\frac{U^2}{a^2}\right)>0$, $q<a$
ρU in ζ-direction	Upwind differencing Eq. (11)	Density biasing based on $\left(1-\frac{a^2}{q^2}\right)$ in Eq. (13)	Shut off density biasing
ρV, ρW in η,ξ directions	Density biasing based on $\left(1-a_{22}\frac{a^2}{V^2}\right)$, $\left(1-a_{33}\frac{a^2}{W^2}\right)$ $\bar{\rho}$ in Eq. (16)	Density biasing based on $\left(1-\frac{a^2}{q^2}\right)$ $\tilde{\tilde{\rho}}$ in Eq. (17)	Shut off density biasing

Table 1. Summary of type-dependent density biasing procedure

IV. Results

As illustrated in Fig. 2, supersonic marching calculations are performed from the nose until an embedded MSR forms. In Fig. 2, the plane AB is the last supersonic marching plane preceding the subsonic bubble and forms the upstream computational boundary for the relaxation calculation. For the first relaxation pass through the subsonic bubble region, θ_{i+1} in Eq. (10) is set equal to θ_i and $(\rho U)_{i+2} = \rho^* q^*$. From the second relaxation cycle on, θ_{i+1}, θ_i, and $(\rho U)_{i+2}$ are computed according to their definitions. A typical supersonic flow with a subsonic bubble calculation required at most only four relaxation cycles (iterating back and forth between planes AB and CD) to obtain a converged location for the bubble. The initial guess, based on the sonic conditions $\rho^* q^*$, worked out very well for all the subsonic bubble cases presented in this paper. The (η,ξ) marching plane can be any arbitrary surface, but for convenience was chosen to be a constant x-plane.

The step size in the marching direction, ζ, for the supersonic part $\left(\left(a_{11}-\frac{U^2}{a^2}\right) < 0,\ q > a\right)$, was automatically chosen by setting the Courant number[5] to be around 5. Once the MSR forms, the eigenvalues become complex, and the step size can not be computed based on a specified Courant number. For marching planes containing the MSR/TSR, the step size was specified into the code depending on the geometry variation. When geometry changes were drastic (region of emergence of a wing from a fuselage), usually a smaller step size $\Delta\zeta$ was required (as small as .003∿.005 for a total length of one) to properly account for rapid changes in the flow. Once the MSR/TSR is fully

ORIGINAL PAGE IS
OF POOR QUALITY

captured and the flow becomes supersonic again, the step size selection once again becomes based on the Courant number. For a pure supersonic flow all the way, the entire calculation could be performed using 40 planes or less ($\Delta\zeta > .025$). However, once an MSR or TSR is present, the total number of ζ planes in the calculation could go as high as 150.

Figure 5 shows the surface pressure distribution in the axial direction on the upper ($\theta = 0$, lee side) and lower ($\theta = 180°$, windward side) plane of symmetry for a developed cross-section forebody geometry reported in Ref. 7. At $M_\infty = 1.7$ and $\alpha = -5°$, the lee side has an embedded MSR which required use of the relaxation operator in Eq. (10). A pure supersonic X-marching for this case would have failed without the MSR treatment described in this paper.

Figure 6 shows the axial pressure distribution on the same geometry for $M_\infty = 2.5$, $\alpha = -5°$. This case has no embedded subsonic bubble and the entire flow remains supersonic in the marching X-direction. The same code is used to generate the results of Figs. 5 and 6. The code automatically turns on the subsonic bubble relaxation treatment without the user having to play a role.

Figure 7 shows the circumferential pressure distribution for the same developed cross-section forebody at $M_\infty = 1.70$, $\alpha = -5°$, and $x/\ell = 0.28$. The embedded MSR thickness is the largest at this axial station. The extent of the subsonic bubble

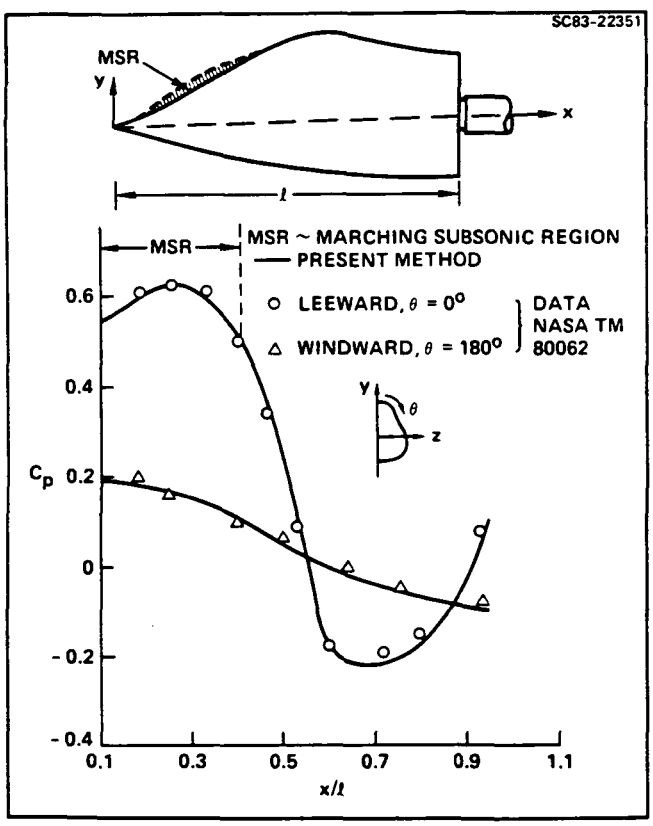

Fig. 5. Axial surface pressure distribution for a developed cross-section forebody; $M_\infty = 1.7$, $\alpha = -5°$.

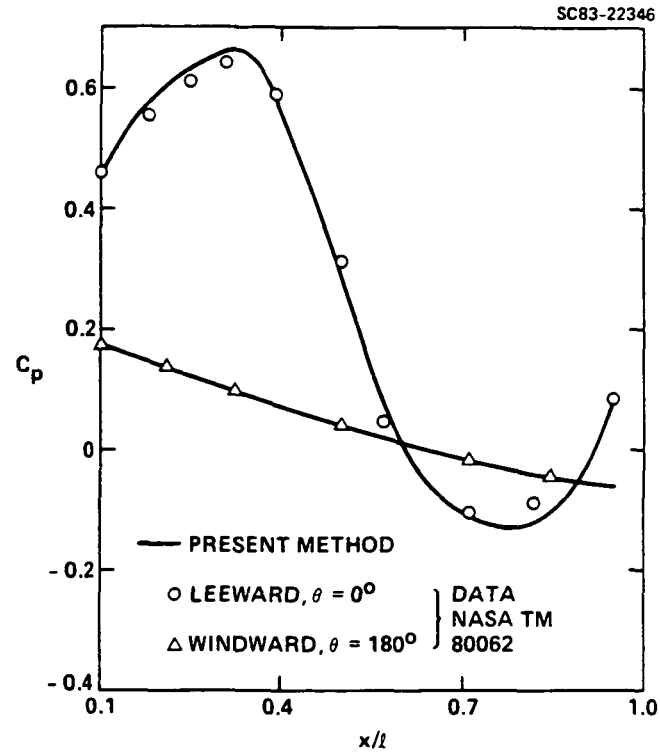

Fig. 6. Axial surface pressure distribution for a developed cross-section forebody; $M_\infty = 2.5$, $\alpha = -5°$. (Fully supersonic flow in the marching direction.)

is marked in Fig. 7. The results of Fig. 5 and Fig. 7 only exhibit MSR, and TSR is not present.

To simulate both the MSR and TSR, a case was constructed with a triple cone geometry. At $M_\infty = 1.6$ and $\alpha = 0°$, this case exhibited the presence of both the MSR and TSR, as shown in Fig. 8. The density biasing is activated in MSR, and turned off automatically in TSR by Eqs. (13) and (17).

For the case of Fig. 9, the pressure distribution in the η direction (away from the body) at an axial station containing the MSR and TSR is shown. The sonic C_p^* at this Mach number is 0.695. Outside of the bow shock, the pressure coefficient C_p goes to zero as shown in Fig. 9.

The axial surface pressure and local Mach number distribution for the triple cone geometry of Fig. 8 are shown in Fig. 10. The MSR and TSR locations are marked. The local Mach number goes below 1 inside the TSR.

Figure 11 shows a supersonic fighter configuration with a wing sweep of around 48°. At a freestream Mach number of 1.6 and $\alpha = 5°$, the leading edge of the wing exhibits an MSR. To solve the flow field over such a fighter configuration, one needs to use the embedded subsonic bubble treatment. Figures 12 and 13 show the surface pressure at various axial stations along with respective grid distribution for the wing-body geometry. The leading edge behaves like a subsonic leading edge, producing a suction peak. For this case, the MSR starts around $x = 0.4$. Figure 14 shows the pressure

ORIGINAL PAGE IS
OF POOR QUALITY

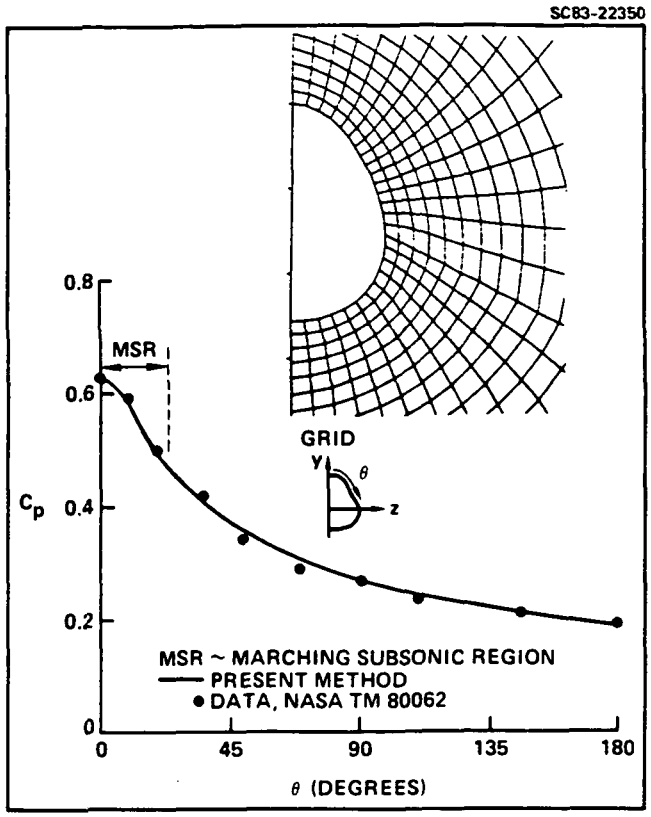

Fig. 7. Circumferential pressure distribution for a developed cross-section forebody; $M_\infty = 1.7$, $\alpha = -5°$, $x/\ell = 0.28$.

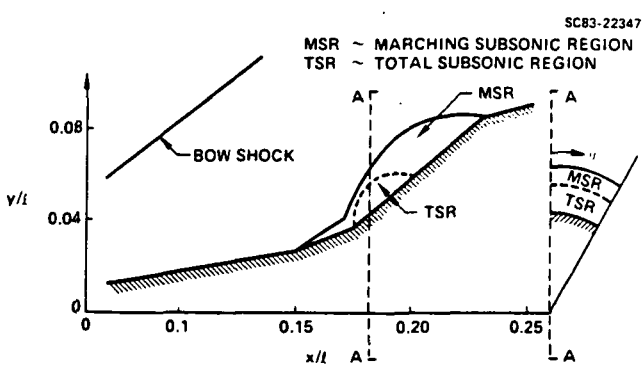

Fig. 8. Marching subsonic and total subsonic regions embedded in a supersonic flow over a typical fuselage-canopy geometry; $M_\infty = 1.6$, $\alpha = 0°$.

distribution for the fighter configuration of Fig. 11 at an axial station $x/\ell = 0.85$, where a wake sheet is present. The grid distribution goes around the wake sheet just like a wing-body case. The approximate wake model described in the paper seems to provide the correct zero pressure jump condition across the wake, as seen in Fig. 14.

Figure 15 shows the pressure distribution right along the leading edge of the fighter configuration. At the axial location where the wing

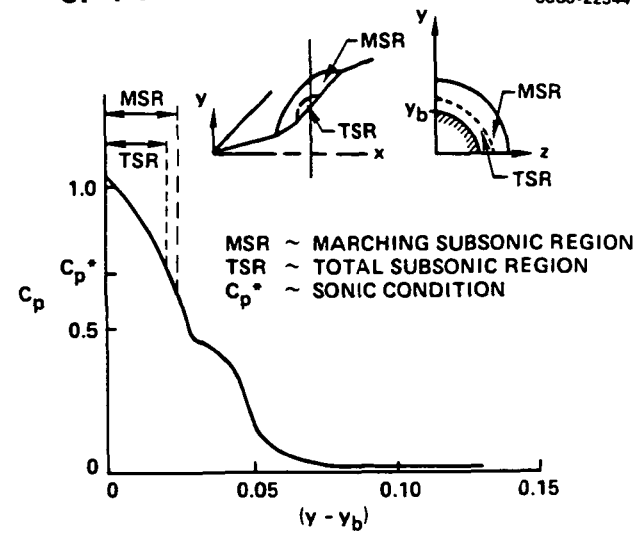

Fig. 9. Pressure distribution away from the fuselage-canopy geometry in the y-direction; $M_\infty = 1.6$, $\alpha = 0°$.

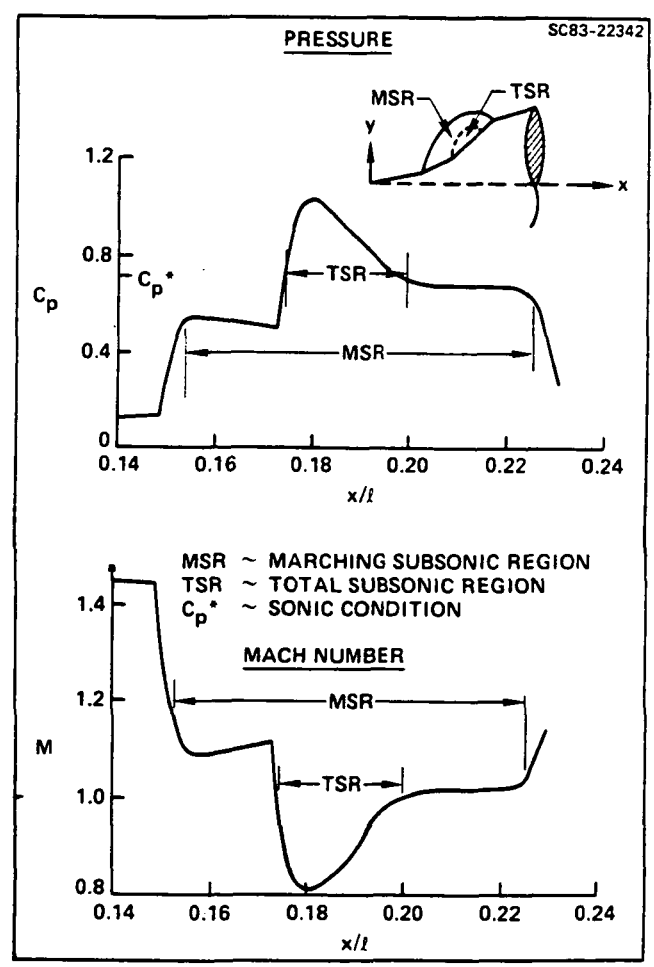

Fig. 10. Axial surface pressure and Mach number distribution on a typical fuselage-canopy geometry.

ORIGINAL PAGE IS
OF POOR QUALITY

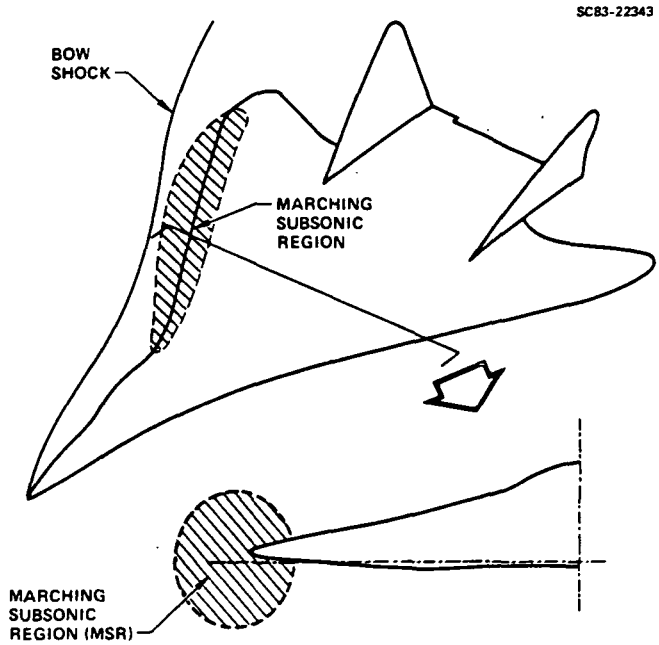

Fig. 11. Supersonic fighter with an embedded marching subsonic region near the leading edge.

emerges from the body, the C_p rises sharply, creating an MSR.

For the wing-body-wake model, at $M_\infty = 1.6$, $\alpha = 5°$, the overall lift coefficient C_L (without the tail) came out to be 0.298, while the tunnel data was 0.277. The overall drag coefficient C_D from the code was 0.0462 (after accounting for a friction drag coefficient value of 0.01077), compared to the tunnel data of 0.0457.

Figure 16 shows the drag prediction capability of the full potential code by demonstrating it on a double wedge delta wing at $M_\infty = 1.62$. At this Mach number, the leading edge exhibited the presence of an MSR for sweep angles less than 60°. A pure supersonic marching code would not have worked for this case. The drag calculation from the full potential code compared very well with the experimental data available in the Princeton Series.

V. Conclusions

A nonlinear full potential method has been developed to treat supersonic flows with embedded subsonic regions. A conservative switching scheme is employed to transition from the supersonic marching algorithm to a subsonic relaxation procedure. The theory of characteristic signal propagation plays a key role in activating various density biasing procedures to produce the necessary artificial viscosity. The method has been shown to produce results which were hitherto not possible using a pure supersonic marching scheme. Currently, work is progressing to treat complex configurations with vertical tails, like the one shown in Fig. 17. The concept of density biasing will also be modified in the future to a flux biasing procedure described in the Appendix.

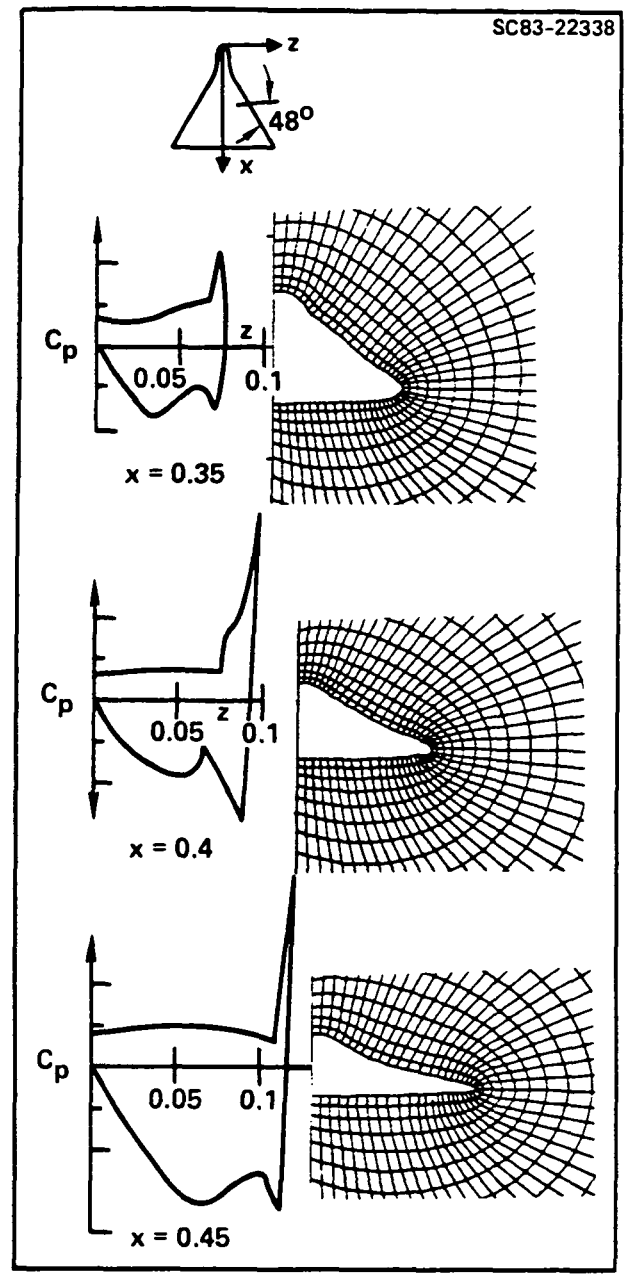

Fig. 12. Pressure distribution on a fighter-like configuration, $M_\infty = 1.6$, $\alpha = 5°$.

Appendix

Flux Biasing Procedure

Based on the work of Hafez and Osher[8], it is possible to modify the density biasing concept to a flux biasing procedure.

Consider the term $\frac{\partial}{\partial \eta}\left(\tilde{\tilde{\rho}}\,\frac{V}{J}\right)$ in Eq. (15). The density biasing procedure defines $\tilde{\tilde{\rho}}$ to be

ORIGINAL PAGE IS
OF POOR QUALITY

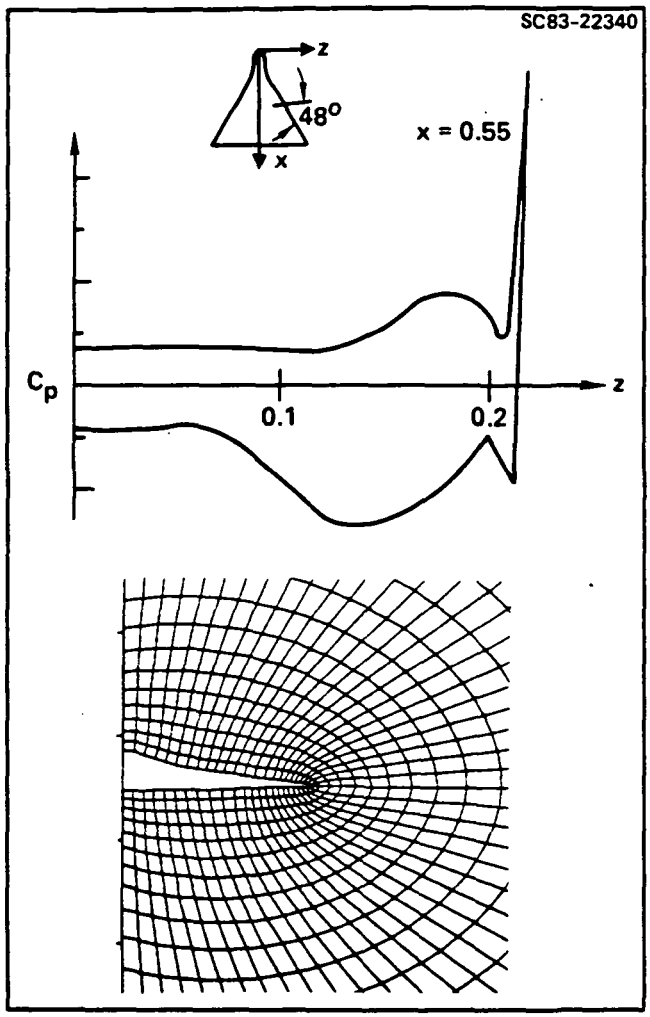

Fig. 13. Pressure distribution on a fighter-like configuration at x = 0.55, $M_\infty = 1.6$, $\alpha = 5°$. The leading edge is in a marching subsonic region.

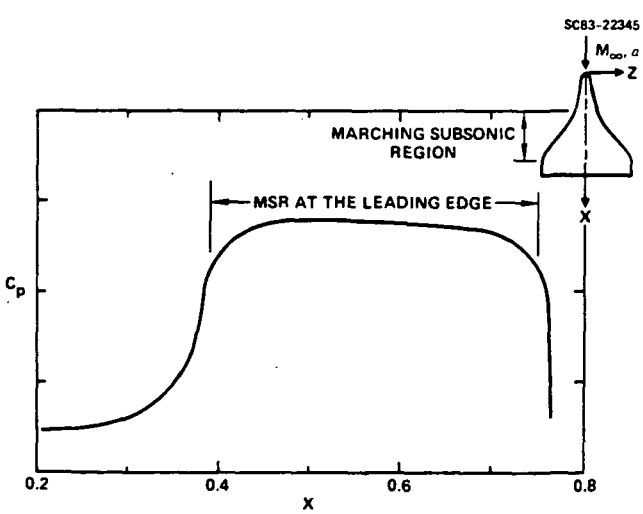

Fig. 15. Pressure distribution along the leading edge of a fighter configuration at $M_\infty = 1.6$, $\alpha = 5°$. The leading edge has a marching subsonic region (MSR).

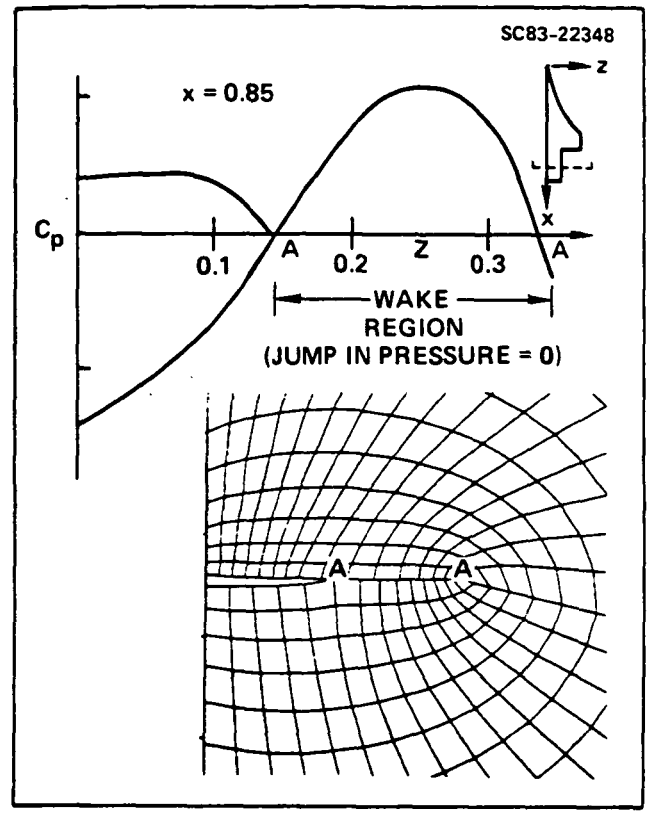

Fig. 14. Grid and pressure distribution in the wake region of a fighter-like configuration, $M_\infty = 1.6$, $\alpha = 5°$, x = 0.85.

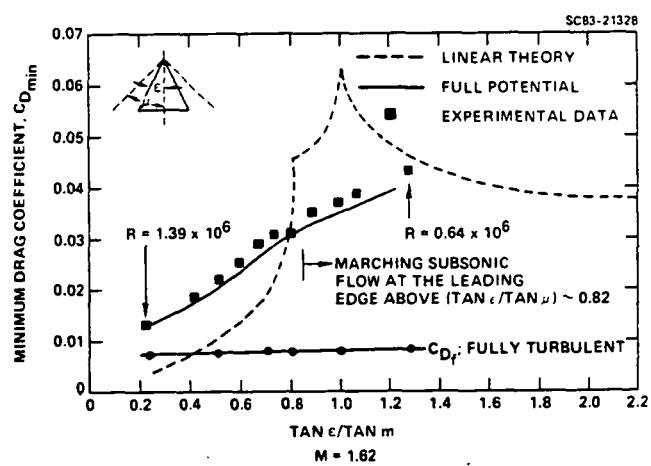

Fig. 16. Drag prediction for a double wedge delta wing at $M_\infty = 1.62$, $\alpha = 0°$. For sweep angles less than 60°, the leading edge has a marching subsonic flow. $C_{D_{min}} = C_{D_f} + C_{D_{inviscid}}$.

ORIGINAL PAGE IS
OF POOR QUALITY

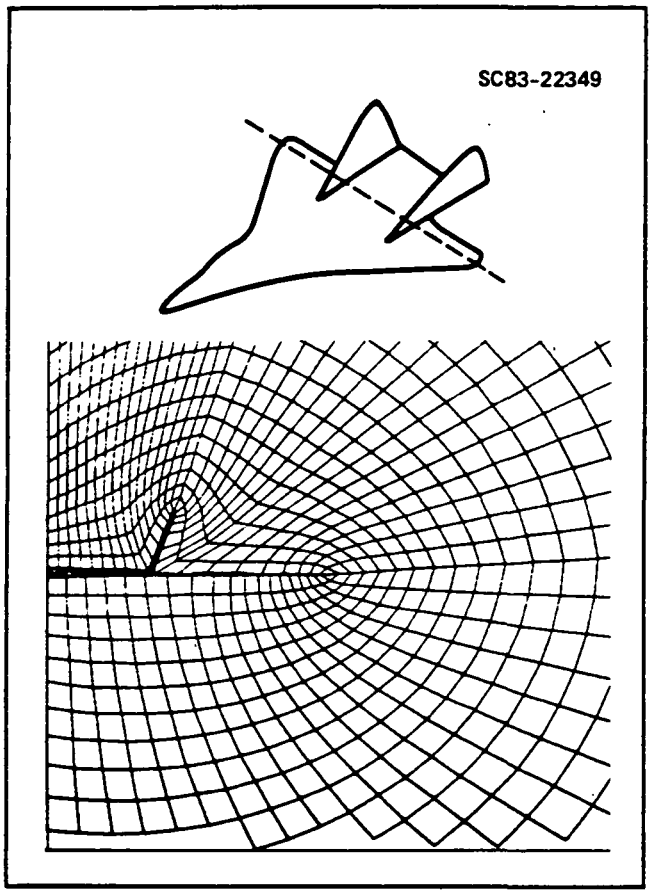

Fig. 17. Wing-vertical tail gridding.

$$\tilde{\tilde{\rho}}_{j+\frac{1}{2}} = (1-\nu)\rho_{j+\frac{1}{2}} + \frac{1}{2}\nu(\rho_j + \rho_{j-1}) \qquad \text{(A1)}$$

where

$$\nu = \max\left(0,\ 1 - \frac{a^2}{q^2}\right).$$

In the flux biasing technique, it will be modified to

$$\frac{\partial}{\partial\eta}\left(\tilde{\tilde{\rho}}\,\frac{V}{J}\right)_{j+\frac{1}{2}} = \frac{\partial}{\partial\eta}\left[\frac{V}{Jq}\left\{\rho q - \Delta\eta\,\frac{\partial}{\partial\eta}(\rho q)_-\right\}\right]_{j+\frac{1}{2}} \qquad \text{(A2)}$$

where

$$(\rho q)_- = 0 \qquad \text{if} \quad q < a$$

$$= (\rho q) - \rho^* q^* \qquad \text{if} \quad q > a\ ,$$

where ρ^* and q^* represent sonic conditions, a is the local speed of sound, and (ρq) is the flux. When the flow is purely subsonic, the flux biasing is turned off automatically.

Acknowledgement

This work was partially supported by NASA-Langley Research Center under Contract NAS1-15820.

References

1. Jameson, A., "Transonic Potential Flow Calculations using Conservation Form," AIAA Second Computational Fluid Dynamics Conference Proceedings, 1975, pp. 148-155.

2. Holst, T.L., "Fast, Conservative Algorithm for Solving the Transonic Full Potential Equation," AIAA Journal, Vol. 18, No. 12, December, 1980, pp. 1431-1439.

3. Siclari, M.J., "Computation of Nonlinear Supersonic Potential Flow over Three-Dimensional Surfaces," AIAA Paper No. 82-0167, presented at the AIAA 20th Aerospace Sciences Meeting, Orlando, Florida, January, 1982.

4. Shankar, V., "A Conservative Full Potential, Implicit, Marching Scheme for Supersonic Flows," AIAA Journal, Vol. 20, No. 11, November, 1982, pp. 1508-1514.

5. Shankar, V. and Osher, S., "An Efficient Full Potential Implicit Method Based on Characteristics for Analysis of Supersonic Flows," AIAA Paper No. 82-0974, June, 1982; also to appear in AIAA Journal, August, 1983.

6. Shankar, V., Rudy, S., and Szema, K.-Y., "Application of a Two-Dimensional Grid Solver for Three-Dimensional Problems," ASME Applied Mechanics, Bioengineering, and Fluids Engineering Conference, Vol. No. G00222, June 20-22, 1983.

7. Townsend, J.C., Howell, D.T., Collins, I.K., and Hayes, C., "Surface Pressure Data on a Series of Analytic Forebodies at Mach Numbers from 1.7 to 4.50 and Combined Angles of Attack and Sideslip," NASA TM 80062, June, 1979.

8. Hafez, M., Whitlow, W., Jr., and Osher, S., "Improved Finite Difference Schemes for Transonic Potential Calculations," in preparation.

ORIGINAL PAGE IS
OF POOR QUALITY

ASME Paper Vol. No. G00222, June 1983

APPLICATION OF A TWO-DIMENSIONAL GRID SOLVER FOR THREE-DIMENSIONAL PROBLEMS

Vijaya Shankar
Manager, Computational Fluid Dynamics Group
Rockwell International Science Center
Thousand Oaks, California

Steve Rudy
Member Technical Staff
Rockwell International NAAO - Columbus Division

and

Kuo-Yen Szema
Member Technical Staff
Rockwell International Science Center
Thousand Oaks, California

Abstract

A two-dimensional elliptic grid solver is presented and its application to various three-dimensional configurations, both internal and external, is demonstrated. The method uses proper forcing terms to cluster grid points near boundaries with a specified grid spacing and allows grid lines to intersect the boundaries at a specified angle. By segmenting the region, grid results are generated for sharp leading edged configurations and wing-vertical tail combinations.

Introduction

An integral part of the Computational Fluid Dynamics work is the development of numerical grid generation procedures for a body-fitted coordinate system as a practical way to apply boundary conditions. Various schemes are available to achieve such a body-fitted system, including conformal mapping,[1] algebraic schemes,[2] elliptic grid solvers,[3-5] and the hyperbolic solver.[6] The method commonly in use is the elliptic grid solver which solves a set of Poisson equations with appropriate right hand side forcing terms to achieve two main features: 1) to cluster points optimally near the boundary and in regions of high gradients in flow, and 2) to force grid lines to intersect the body surface and other computational boundaries in a nearly orthogonal fashion. In elliptic grid solvers the quality of the grid distribution critically depends on the choice of the forcing terms.

The purpose of this paper is to illustrate the effective use of one such elliptic solver with suitable forcing terms, in developing computational grid for a wide variety of both internal and external three-dimensional problems. Examples to be shown in this paper include grid generation for a three-dimensional inlet (both interior and exterior of the inlet), external grid for a sharp leading edged wing-body and wing-vertical tail combinations, and grid for multiple-connected regions of an arrow wing-body configuration. The key result in the paper is the grid generation for a three-dimensional inlet by using just a two-dimensional grid solver.

The elliptic grid solver to be presented here is somewhat similar to that of Ref. 5, but differs considerably in the implementation of a proper procedure for the evaluation of the forcing terms.

Formulation

Thompson et al.[3] have proposed the following inhomogeneous Laplace equations as the governing system for grid generation

$$\xi_{xx} + \xi_{yy} = P(\xi,\eta)$$

$$\eta_{xx} + \eta_{yy} = Q(\xi,\eta) \quad . \tag{1}$$

Equation (1) represents the transformation from the (x,y) physical domain to the (ξ,η) computational plane. The right hand side of Eq. (1) defines the forcing terms to achieve a desired grid distribution. Various grid generation methods[3-5] differ from each other in the choice and implementation of appropriate P and Q source terms to provide desired grid properties. The purpose of this paper is to describe an efficient and automated procedure for choosing the proper forms of P and Q to achieve grid clustering and grid orthogonality near surfaces.

Interchanging the role of dependent (ξ,η) and independent (x,y) variables, in the transformed space, Eq. (1) takes the form

$$\alpha x_{\xi\xi} - 2\beta x_{\xi\eta} + \gamma x_{\eta\eta} = -J^2(Px_\xi + Qx_\eta)$$

$$\alpha y_{\xi\xi} - 2\beta y_{\xi\eta} + \gamma y_{\eta\eta} = -J^2(Py_\xi + Qy_\eta) \tag{2}$$

where $\alpha = x_\eta^2 + y_\eta^2$, $\beta = x_\xi x_\eta + y_\xi y_\eta$, $\gamma = x_\xi^2 + y_\xi^2$ and $J = x_\xi y_\eta - y_\xi x_\eta$.

Choosing the following forms for P and Q

ORIGINAL PAGE IS
OF POOR QUALITY

$$P = J^2\phi(\xi,\eta)\alpha$$

$$Q = J^2\psi(\xi,\eta)\gamma \quad , \tag{3}$$

Equation (2) takes the form

$$\alpha(x_{\xi\xi} + \phi x_\xi) - 2\beta x_{\xi\eta} + \gamma(x_{\eta\eta} + \psi x_\eta) = 0$$

$$\alpha(y_{\xi\xi} + \phi y_\xi) - 2\beta y_{\xi\eta} + \gamma(y_{\eta\eta} + \psi y_\eta) = 0 \quad . \tag{4}$$

Equation (4) contains two free parameters, ϕ and ψ. Referring to Fig. 1, the role of these parameters is to enforce two conditions that the grid lines have to satisfy. 1) Maintain a given ΔS grid spacing in the transverse direction (η) at the surface $\eta = \eta_b$, and 2) provide a specified intersecting angle θ between the surface ($\eta = \eta_b$) and the transverse coordinate (ξ = constant). Solving for ϕ and ψ from Eq. (4), one gets

$$\phi = -\frac{1}{J}(y_\eta x_{\xi\xi} - x_\eta y_{\xi\xi}) + \frac{2\beta}{\alpha J}(x_{\xi\eta}y_\eta - y_{\xi\eta}x_\eta) - \frac{\gamma}{\alpha J}(y_\eta x_{\eta\eta} - x_\eta y_{\eta\eta})$$

$$\psi = \frac{1}{J}(x_{\eta\eta}y_\xi - y_{\eta\eta}x_\xi) - \frac{2\beta}{\gamma J}(x_{\xi\eta}y_\xi - y_{\xi\eta}x_\xi) + \frac{\alpha}{\gamma J}(x_{\xi\xi}y_\xi - y_{\xi\xi}x_\xi) \quad . \tag{5}$$

Equation (5) is valid at every grid point. However, the evaluation of ϕ and ψ requires values for all the derivatives x_η, x_ξ, y_η, y_ξ, $x_{\xi\xi}$, $x_{\eta\eta}$, $y_{\xi\xi}$, $y_{\eta\eta}$, $x_{\xi\eta}$ and $y_{\xi\eta}$. One can, however, solve for ϕ and ψ on the surface ($\eta = \eta_b$) in Fig. 1, by prescribing the ΔS and θ values in the following manner:

1. Specify the intersecting angle θ between the transverse grid line (ξ = constant) and the body surface ($\eta = \eta_b$). This condition can be written as

$$\nabla\xi\cdot\nabla\eta = |\nabla\xi||\nabla\eta| \cos\theta \quad . \tag{6}$$

In the transformed space, Eq. (6) takes the form

$$x_\xi x_\eta + y_\xi y_\eta = -[(x_\eta^2 + y_\eta^2)(x_\xi^2 + y_\xi^2)]^{1/2} \cos\theta \quad . \tag{7}$$

2. Specify the grid spacing ΔS at the boundary ($\eta = \eta_b$) in the transverse direction (ξ = constant). This condition can be stated in the form

$$S_\eta = \sqrt{x_\eta^2 + y_\eta^2} \quad . \tag{8}$$

Using Eqs. (7) and (8) and the relationship $\nabla\xi \times \nabla\eta = |\nabla\xi||\nabla\eta|\sin\theta$, one can write the following relationships along the body surface $\eta = \eta_b$.

$$(x_\eta)_{\eta=\eta_b} = S_\eta(-x_\xi \cos\theta - y_\xi \sin\theta)/\sqrt{x_\xi^2 + y_\xi^2}$$

$$(y_\eta)_{\eta=\eta_b} = S_\eta(-y_\xi \cos\theta + x_\xi \sin\theta)/\sqrt{x_\xi^2 + y_\xi^2} \tag{9}$$

where θ and S_η are specified by the user. Once the grid points along $\eta = \eta_b$ (body surface) are prescribed, the differential operators x_ξ, y_ξ, $x_{\xi\xi}$, $y_{\xi\xi}$ appearing in Eq. (5) can be evaluated at the body surface ($\eta = \eta_b$) using the following relationships (refer to Fig. 1 for notation)

$$x_{\eta\eta} = (-7x_1 + 8x_2 - x_3)/2\Delta\eta^2 - 3(x_\eta)_{\eta=\eta_b}/\Delta\eta$$

$$y_{\eta\eta} = (-7y_1 + 8y_2 - y_3)/2\Delta\eta^2 - 3(y_\eta)_{\eta=\eta_b}/\Delta\eta \tag{10}$$

where $(x_\eta)_{\eta=\eta_b}$ and $(y_\eta)_{\eta=\eta_b}$ are obtained from Eq. (9). Using the derivative values from Eqs. (9) and (10), the expressions for ϕ and ψ given by Eq. (5) can be precisely computed along the boundary $\eta = \eta_b$. The same procedure is repeated along all the boundaries of the computational domain to obtain the boundary variation of ϕ and ψ. Once ϕ and ψ values are known along the computational boundaries, their values at interior mesh points are computed by interpolation. Usually $\theta = \pi/2$ is used in Eq. (7) to achieve nearly orthogonal grid lines at the boundaries. The use of transverse direction derivatives x_η, y_η, $x_{\eta\eta}$, $y_{\eta\eta}$, $x_{\eta\xi}$ and $y_{\eta\xi}$ in the evaluation of ϕ and ψ in Eq. (5) makes the procedure of this paper considerably different from the technique of Ref. 5. The ϕ and ψ values along boundaries are continuously updated after each grid relaxation cycle, in a manner similar to the procedure in Ref. 4.

The procedure described so far generates a two-dimensional grid in the x,y plane. If the boundary, say $\eta = \eta_b$ in Fig. 1, is not confined to a two-dimensional plane, that is, along $\eta = \eta_b$, all x, y and z are specified as shown in Fig. 2. Then, one can generate a warped computational plane that contains the boundary $\eta = \eta_b$ in the following manner:

1) First solve for x,y from Eq. (4). This provides x,y grid in the projected plane, shown in Fig. 2.

2) Then solve the Laplace equation

$$z_{xx} + z_{yy} = 0 \tag{11}$$

with z prescribed along boundaries. In the transformed space, Eq. (11) becomes

$$\alpha(z_{\xi\xi} + \phi z_\xi) - 2\beta z_{\xi\eta} - \gamma(z_{\eta\eta} + \psi z_\eta) = 0 \quad . \tag{12}$$

Solution to Step (1) above provides values of α,β,γ,ϕ and ψ that are required in solving Eq. (12).

The grid results to be presented in this paper are obtained by solving Eqs. (4) and (12) simultaneously. The method has been effectively used to generate both

the internal and external grid for a three-dimensional inlet system, and also the external grid for varieties of sharp leading edged wing-body combinations. A typical grid calculation required approximately 100 relaxation cycles to converge the residual to 10^{-8} level.

Results

First external grid results are presented for sharp leading edged configurations, wing-vertical tail combinations and then grid results for a three-dimensional inlet are shown.

External Grid

In the present study, the external grid for a wing-body combination is generated for use in a supersonic flow calculation by a marching technique.[7] This requires grid generation in every marching plane, which can be either a constant z plane or a spherical plane. Figure 3 shows the schematic of a sharp leading edged wing-body cross section. To be able to accommodate sharp edges in the grid generation routine, a cut A-B in Fig. 3 is made and the regions 1-2-B-A-1 and 3-A-B-4-3 are treated separately with a given grid distribution along the cut A-B.

Figure 4 shows a double-wedge delta wing and the grid generated at various axial cuts of the geometry. Figure 5 shows the pressure contours at a typical axial station of the geometry in Fig. 4 indicating the presence of a shock and expansion fans at $M = 1.92$, $\alpha = 0°$. Figure 6 shows the minimum drag results for zero lift and comparison with experimental data. The success of a good flow calculation such as the one shown in Fig. 6 critically depends on the quality of the grid.

Figure 7 shows the grid generated for an arrow wing-body combination. The cross section starts initially as a wing alone, then transitions to a wing-body, and finally becomes a detached wing-body. The grid generation routine is general enough to accommodate such a shape change in the axial direction. Flow calculations obtained for the arrow wing-body combination using the grid of Fig. 7 are shown in Fig. 8. Improvements to the wake treatment for the methodology of Ref. 7 are currently underway.

Figure 9 shows the schematic of a typical fighter configuration and grid results at various axial locations. By segmenting the entire region, the present grid solver can be effectively used to generate grid around wing-vertical tail combinations. Figure 10 shows the gridding for a sharp leading edged Sears-Haack wing-body combination.

Three-Dimensional Inlet Grid

Figure 11 shows a schematic of a three-dimensional inlet embedded in a global computational domain. The objective is to develop a body-fitted coordinate system both on the exterior and the interior of the inlet. The leading edge of the inlet (1-2-3-4-5-6-7-1 in Fig. 11) is highly swept and curved. The intent is to perform a Navier-Stokes calculation for that geometry, which will require a clustered grid near the leading edge as well as near the walls of the inlet. To create a clustered body-fitted as well as leading edge fitted grid system, it was decided to gradually rotate the upstream constant z plane such that there will be leading edge plane containing the entire leading edge 1-2-3-4-5-6-7-1. This warped leading edge plane would then be gradually rotated to a constant z downstream plane. In order to achieve this, first series of loops were created starting from the leading edge to the downstream plane as shown in Fig. 12. For each loop, the inner and outer inlet wall geometry in terms of (x,y,z) was prescribed as shown in Fig. 13. Then, for each loop a warped plane containing the body-fitted grid system was generated using the x,y grid solver procedure of Eq. 4 and then a "z" value at each grid point from Eq. (12).

Figure 14 shows a loop near the leading edge of the inlet, a perspective view of the warped body-fitted grid surface, and a constant z projected plane showing the details of the interior and the exterior grid. Figure 15 shows an enlarged view of the upper and lower left hand corner region of the inlet. Figure 16 shows a loop at a mid-station location of the inlet clearly indicating the thickness of the inlet wall. Also shown in Fig. 16 are the perspective view of the warped body-fitted surface and a z-plane projected grid. Figure 17 shows the grid at a final downstream plane for the inlet.

Figures 11 to 17 represent three-dimensional inlet grid work obtained purely by using two-dimensional grid solvers based on Eqs. (4) and (12). Currently, this inlet grid is being incorporated into a three-dimensional Navier-Stokes code.

Conclusions

This paper presents an elliptic grid solver in two dimensions with proper forcing terms to obtain certain desired grid qualities such as grid clustering and orthogonality near body surfaces. The procedure has been successfully applied to various three-dimensional external sharp leading edged configurations as well as for a three-dimensional inlet.

Acknowledgement

Partial funding of this work was provided by NASA-Langley Research Center under Contract NAS1-15820.

References

1. Moretti, G., "Extended Conformal Mappings for Supersonic Aircraft Calculations," Poly-AG-AM Report 76-8, 1976.
2. Eiseman, P.R., "Three-dimensional Coordinates About Wings," AIAA Paper No. 79-1461.
3. Thompson, J. F., Thames, F. C. and Mastin, C. W., "Automatic Numerical Generation of Body-fitted Curvilinear Coordinate System for Field Containing Any Number of Arbitrary Two-Dimensional Bodies," J. Comp. Phys., Vol. 15, No. 3, July 1974.
4. Steger, J. L. and Sorenson, R. L., "Automatic Mesh-Point Clustering Near a Boundary in Grid Generation with Elliptic Partial Differential Equations," Journal of Computational Physics, Vol. 33, No. 3, December 1979, pp. 405-410.
5. Thomas, P. D. and Middlecoff, J. F., "Direct Control of the Grid Point Distribution in Meshes Generated by Elliptic Equations," AIAA Journal, Vol. 18, No. 6, June 1980.
6. Steger, J. L. and Chaussee, D. S., "Generation of Body-fitted Coordinates Using Hyperbolic Partial Differential Equations," FSI Report 80-1, January 1980.
7. Shankar, V. and Osher, S., "An Efficient Full Potential Implicit Method Based on Characteristics for Analysis of Supersonic Flows," AIAA Paper No. 82-0974.

ORIGINAL PAGE IS
OF POOR QUALITY

ORIGINAL PAGE IS
OF POOR QUALITY

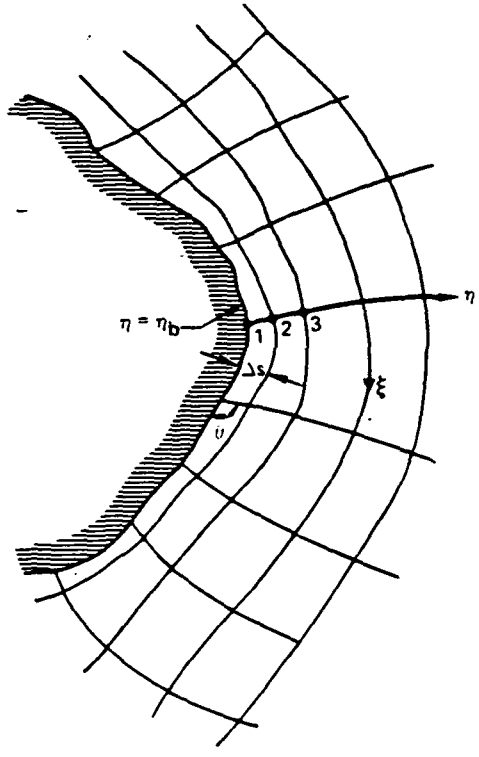

Fig. 1 Notation for the grid solver.

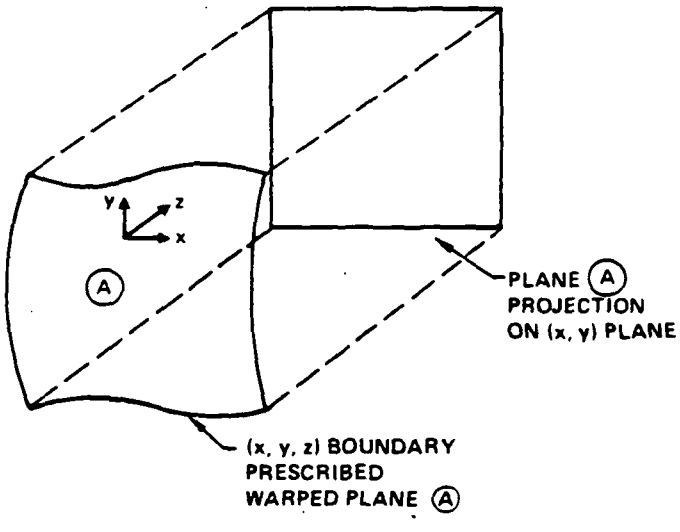

Fig. 2 Grid generation on a curved surface.

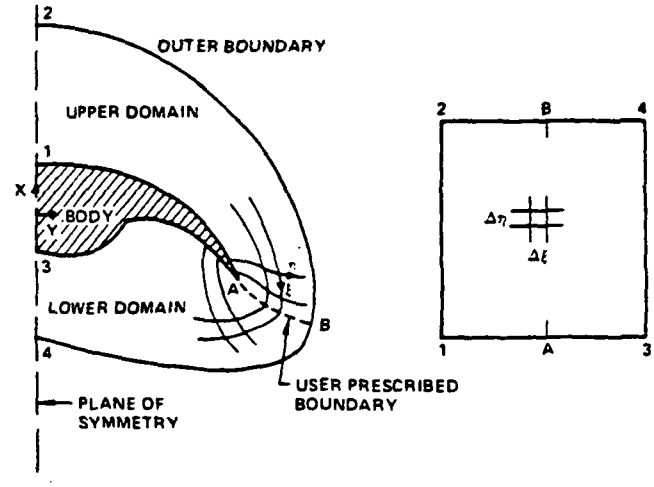

Fig. 3 Schematic of a sharp leading edged wing-body cross section.

ORIGINAL PAGE IS
OF POOR QUALITY

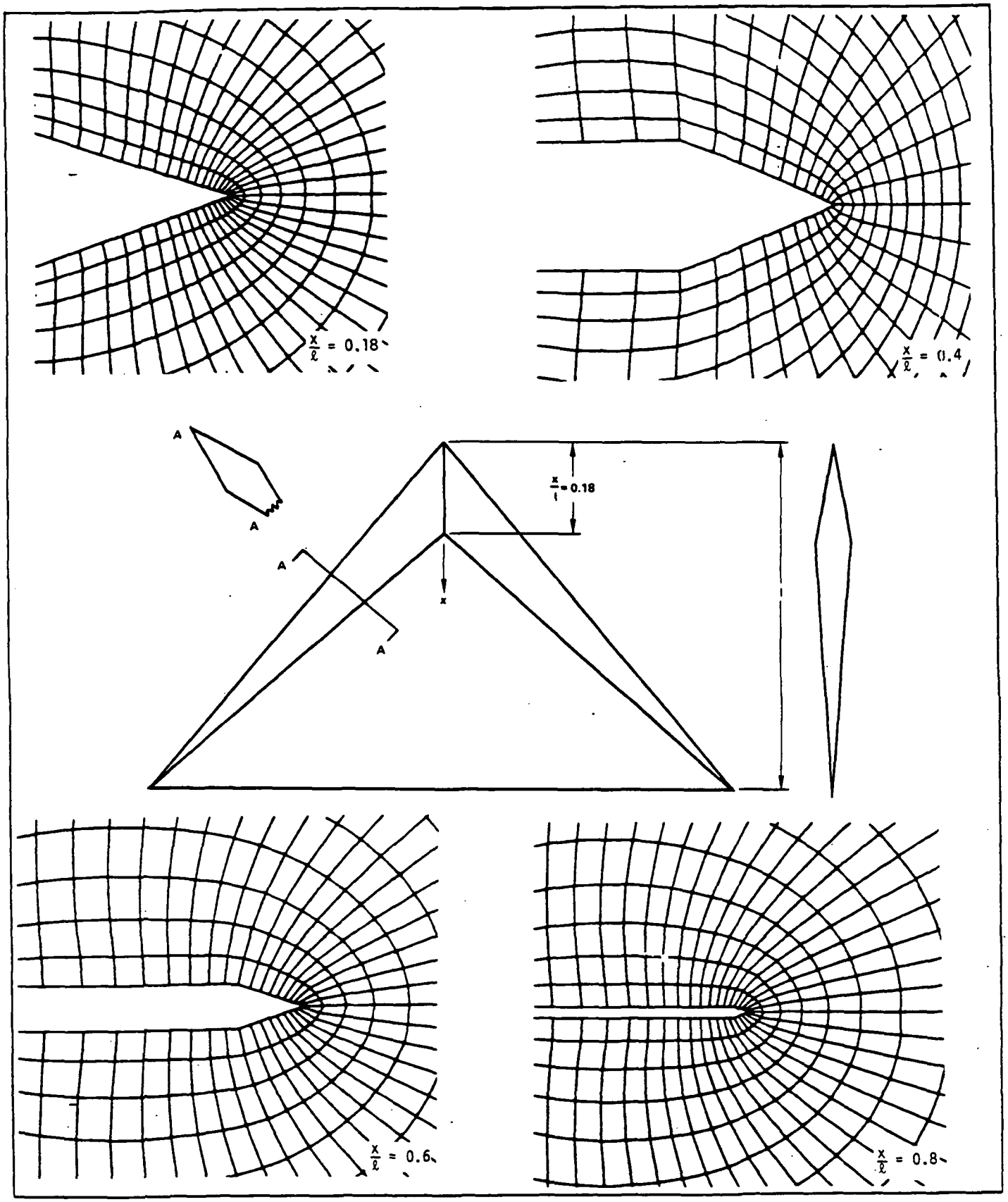

Fig. 4 Gridding for a double wedged delta wing.

ORIGINAL PAGE IS
OF POOR QUALITY

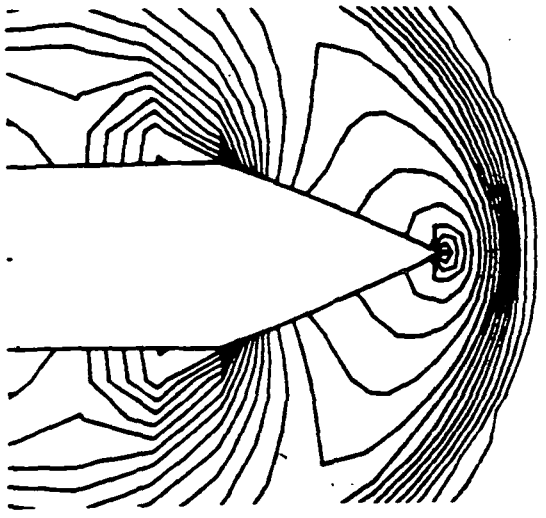

Fig. 5 Pressure contours at $x/\ell = 0.4$ for the delta wing at $M_\infty = 1.92$ and zero degree angle of attack.

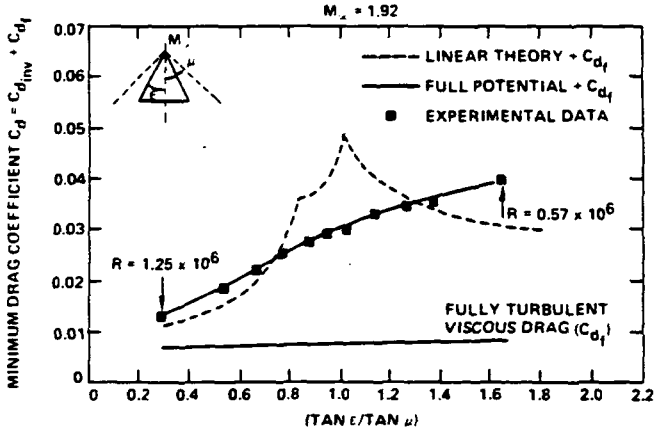

Fig. 6 Minimum drag coefficients for the delta wing and comparison with experimental data.

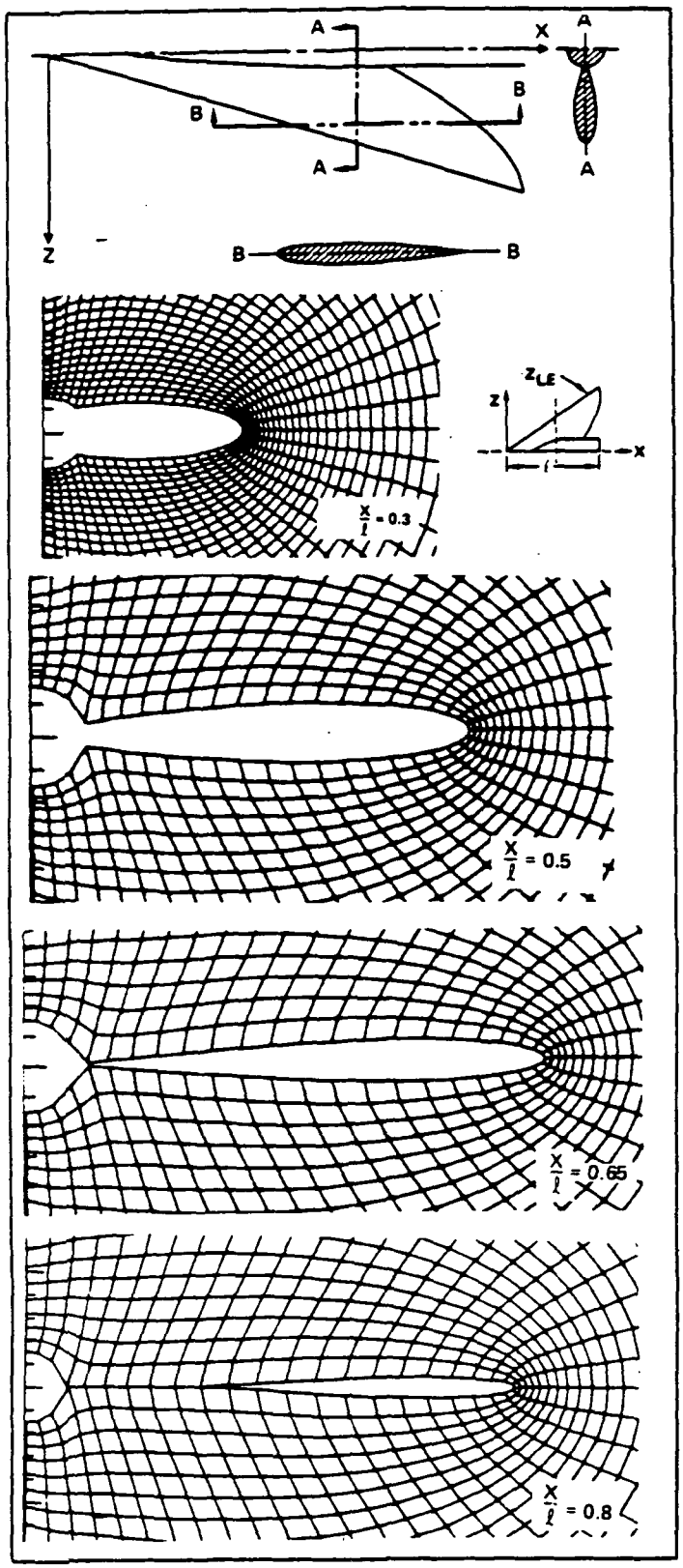

Fig. 7 Gridding for an arrow wing-body combination.

ORIGINAL PAGE IS
OF POOR QUALITY

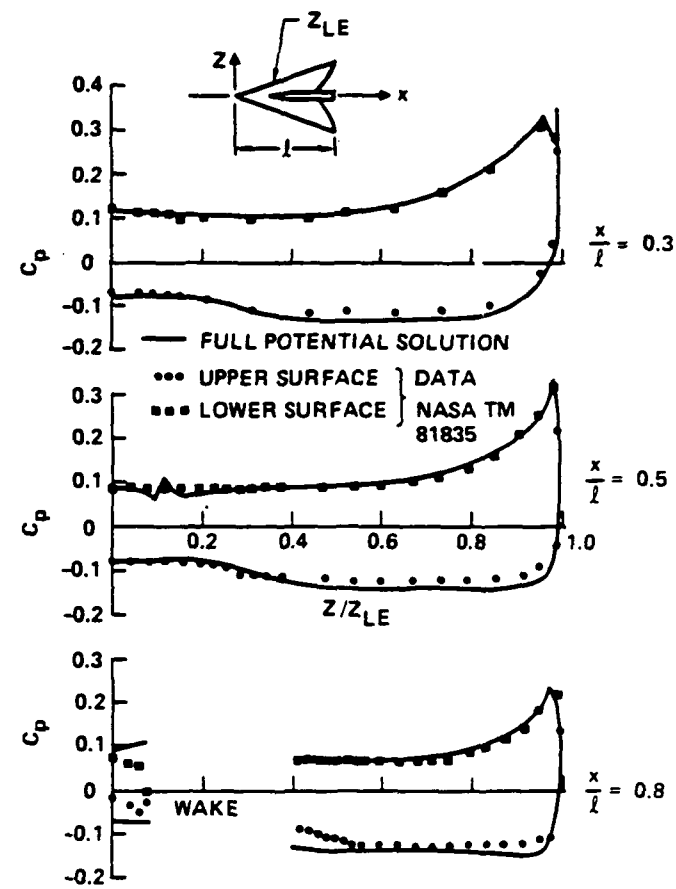

Fig. 8 Flow calculations for the arrow wing-body configuration at M_∞ = 2.96 and α = 10.01°.

ORIGINAL PAGE IS
OF POOR QUALITY

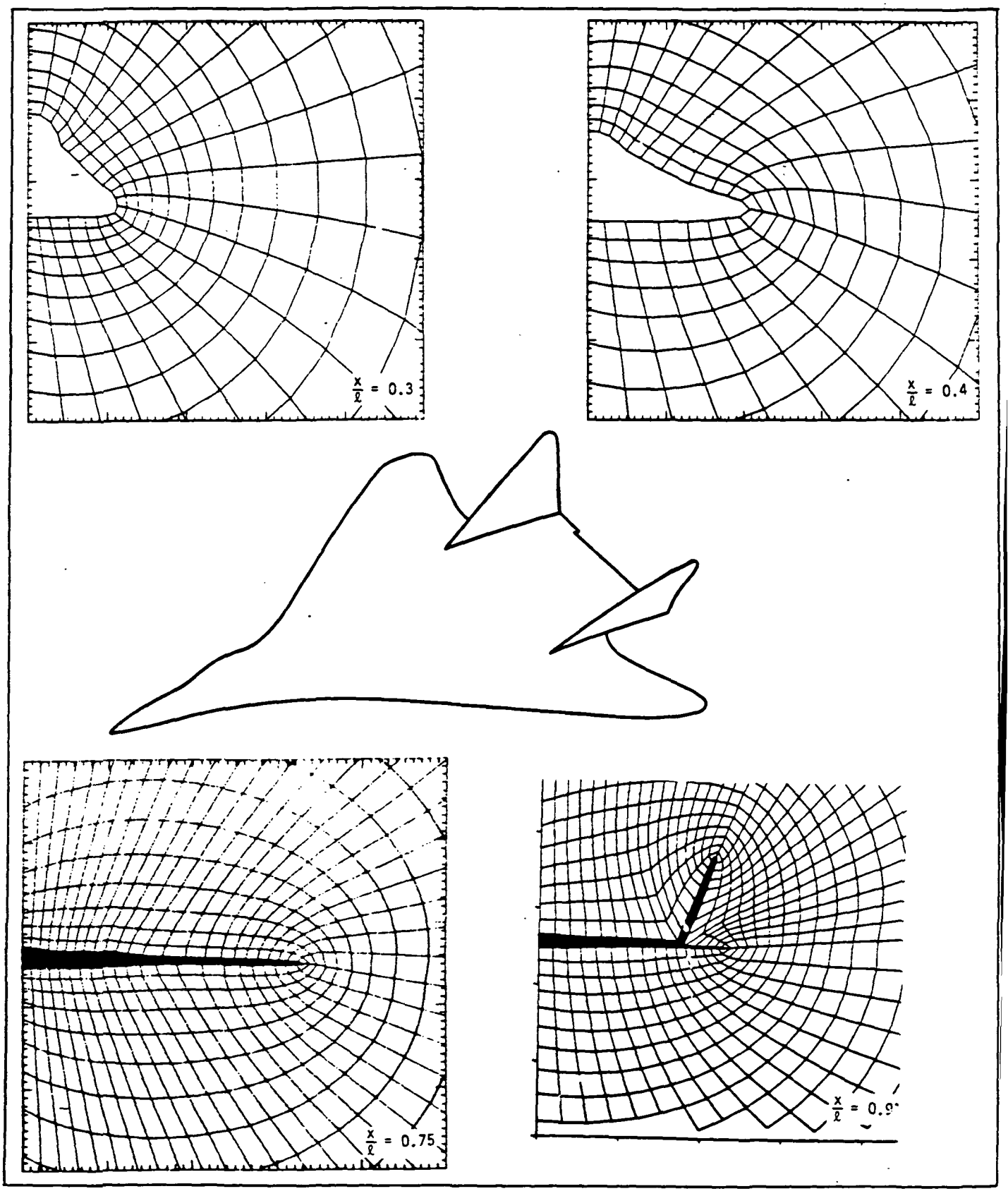

Fig. 9 Gridding for a typical fighter configuration with vertical tails.

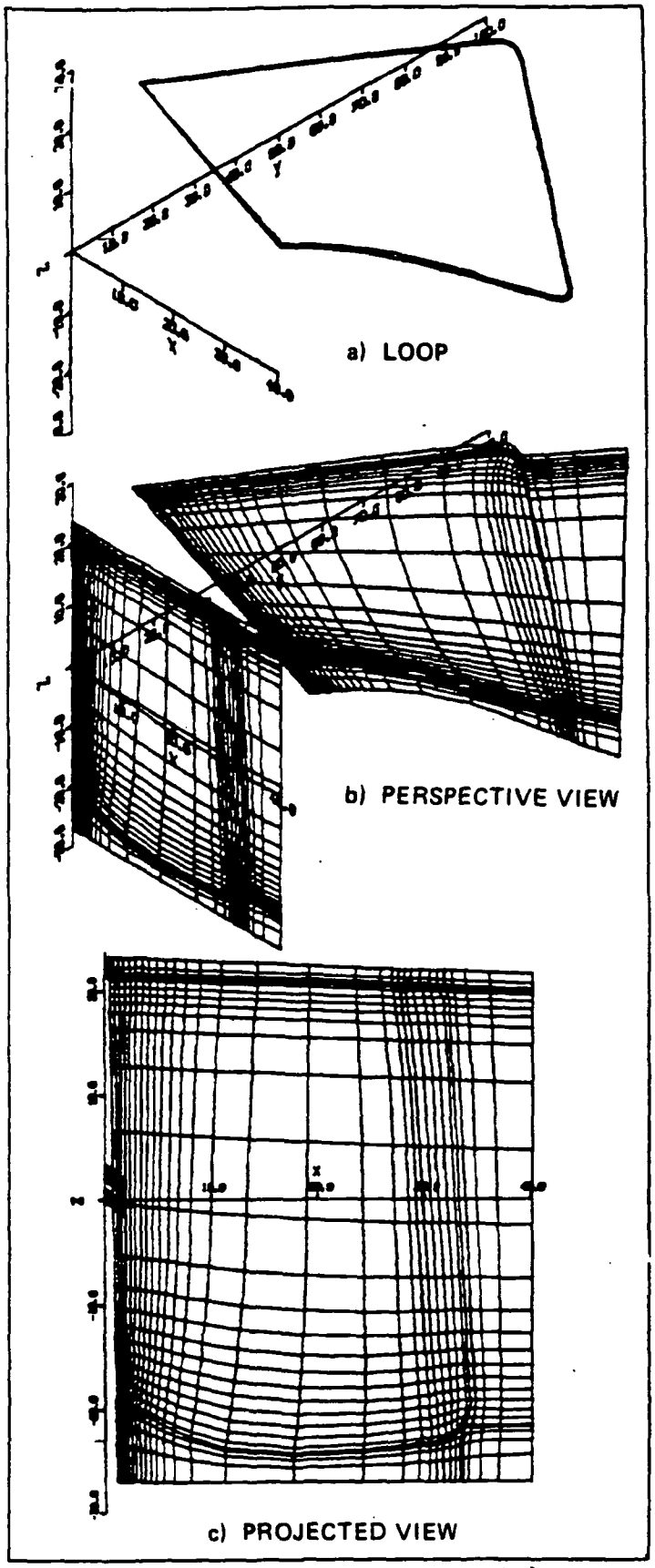

Fig. 14 Body-fitted grid system on a warped plane near the inlet leading edge.

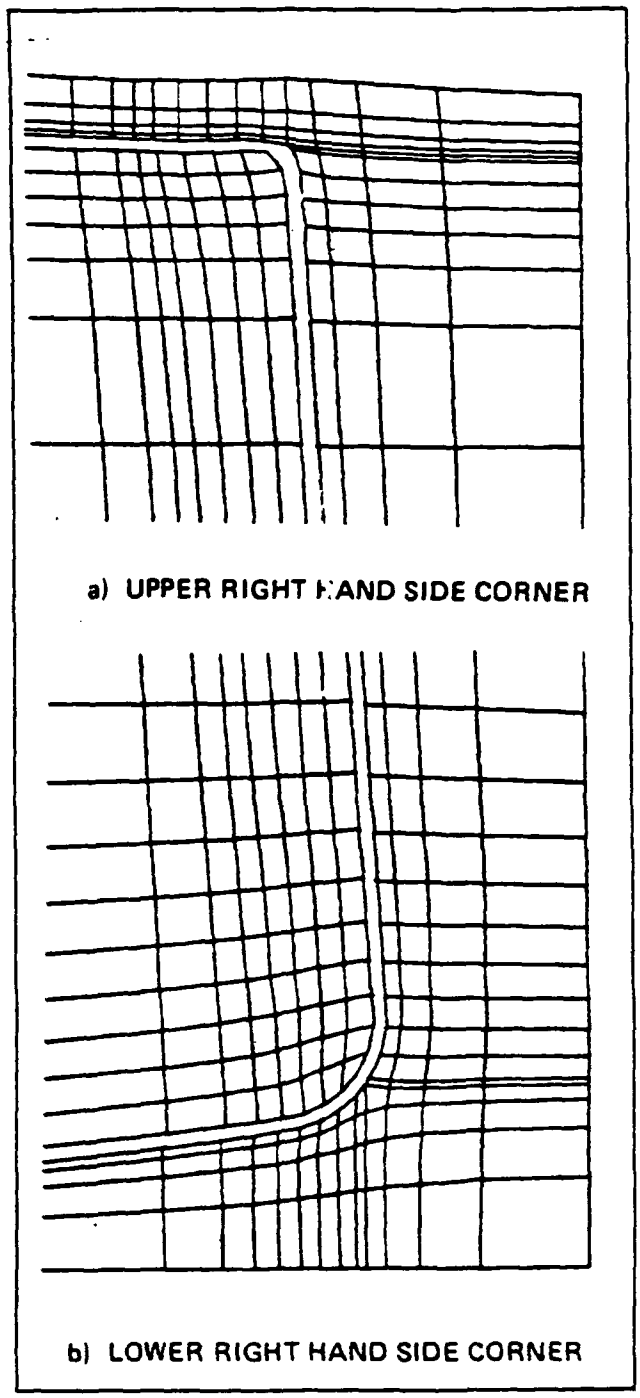

Fig. 15 Enlarged views of the body-fitted coordinate system near corners of the inlet.

ORIGINAL PAGE IS
OF POOR QUALITY

ORIGINAL PAGE IS
OF POOR QUALITY

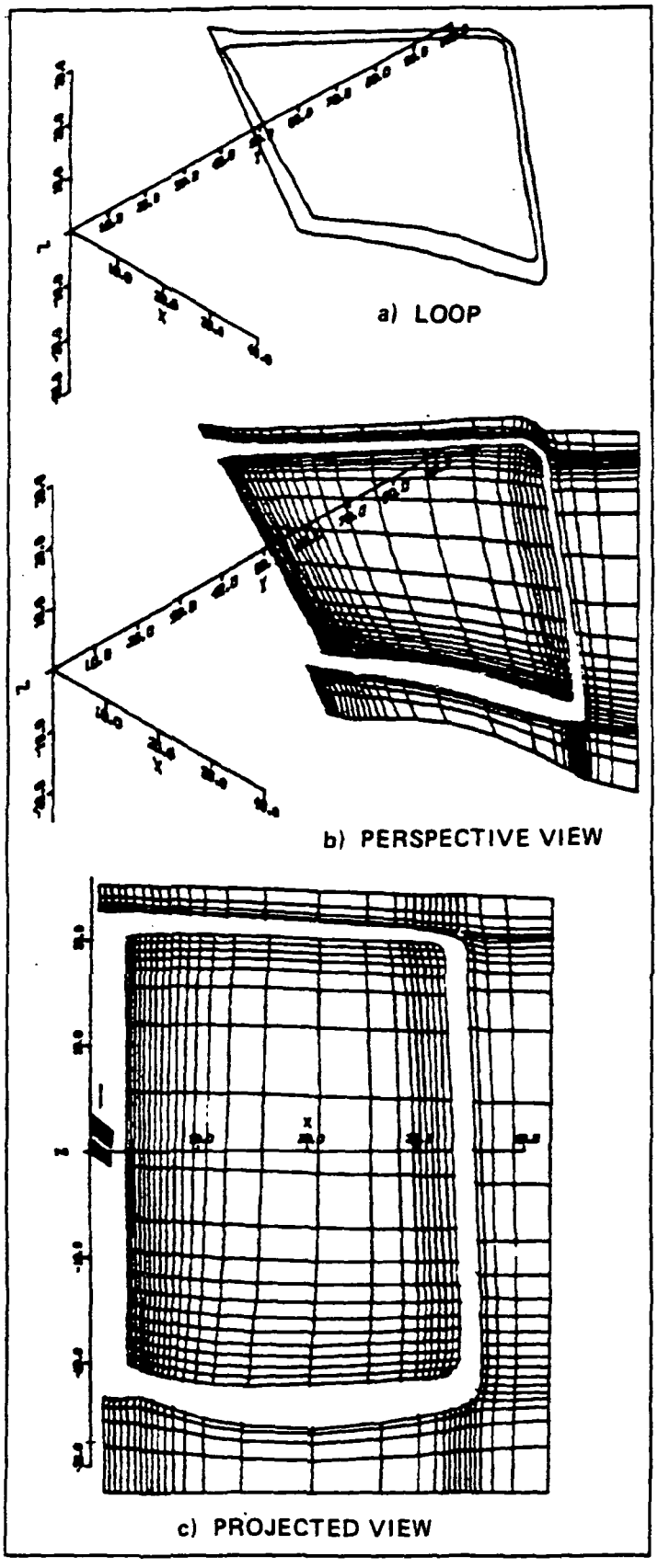

Fig. 16 Body-fitted grid system at the mid station of the inlet.

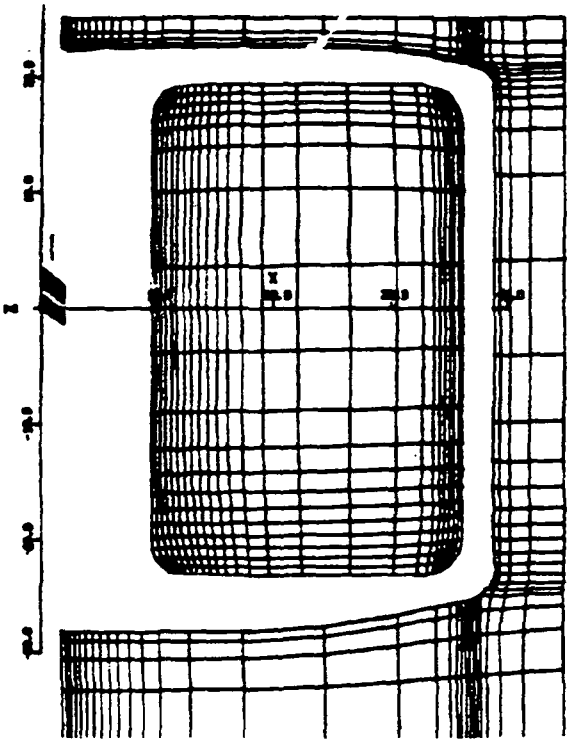

Fig. 17 Body-fitted grid system at the final downstream plane.

ORIGINAL PAGE IS
OF POOR QUALITY

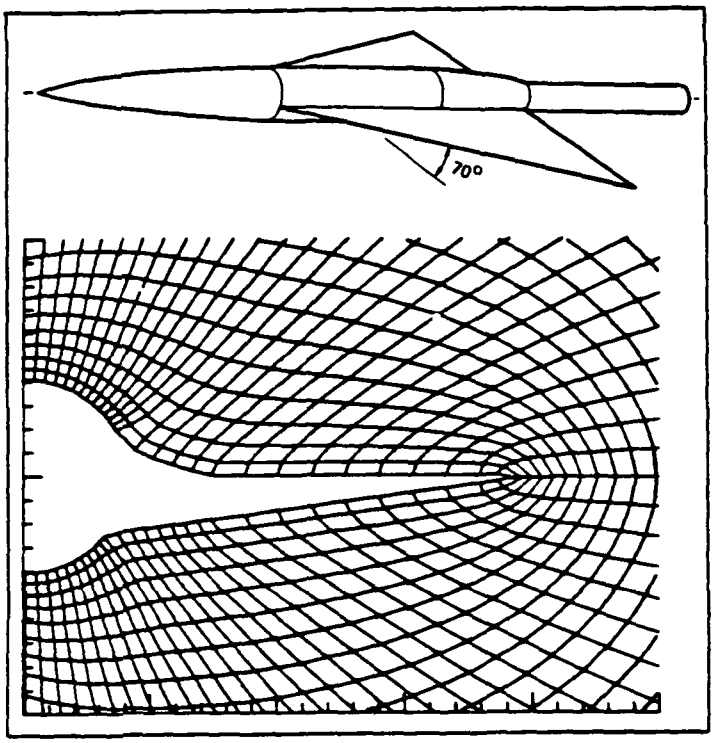

Fig. 10 Gridding for a sharp leading-edged wing-body combination.

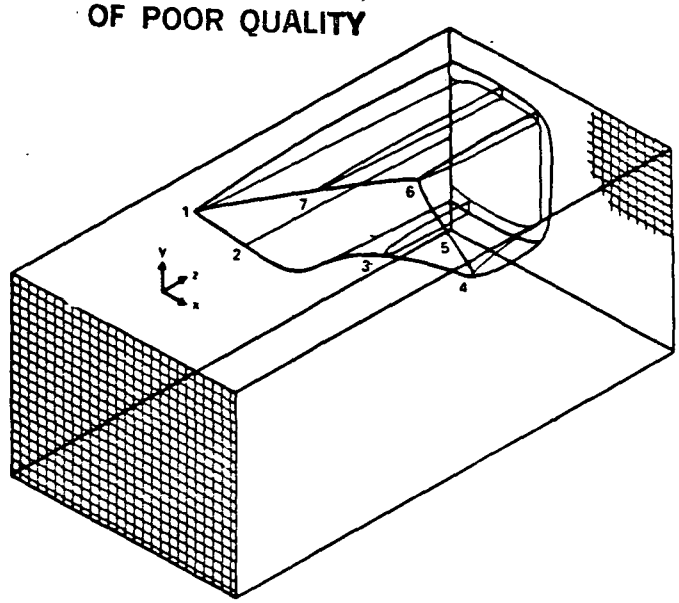

Fig. 11 Schematic of a three-dimensional inlet.

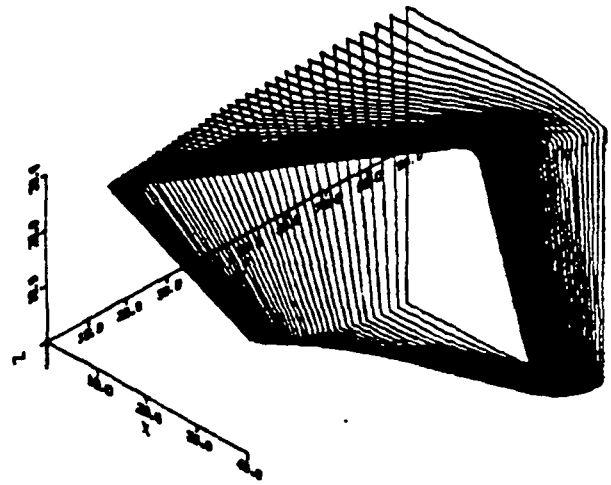

Fig. 12 Construction of inlet loops.

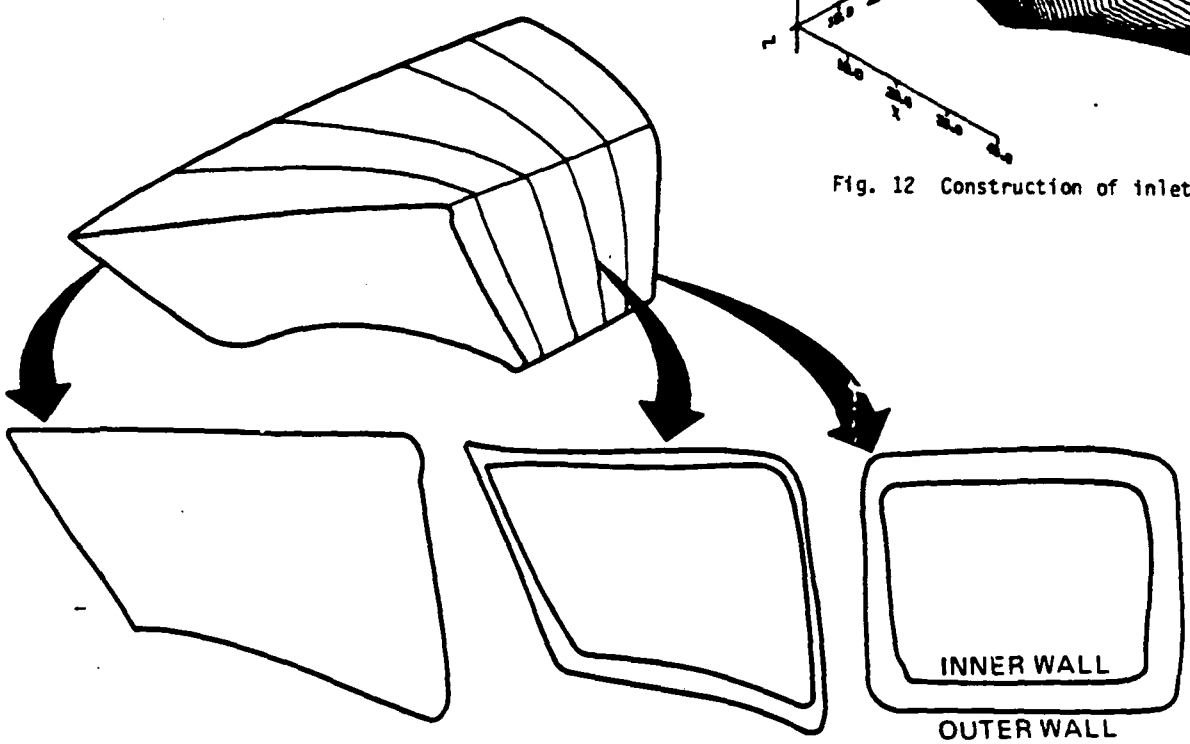

Fig. 13 Inner and outer wall shapes of the inlet at various loop locations.